



# Adjoint volume-of-fluid approaches for the hydrodynamic optimisation of ships

Jörn Kröger\*, Niklas Kühl and Thomas Rung

Fluid Dynamics and Ship Theory (M8), Hamburg University of Technology (TUHH), Hamburg, Germany

## ABSTRACT

The paper is concerned with simulation-based shape optimisation in marine engineering flows. Attention is devoted to the derivation of an adjoint complement to two-phase flow finite-volume procedures. The strategy refers to an extension of a hybrid continuous/discrete adjoint method for volume-of-fluid (VoF) approaches. The study outlines means to formulate a discrete adjoint VoF scheme from the terms that originate from variations of the fluid properties. The adjoint solution is verified against results of a direct differentiation technique. The application is devoted to the drag optimisation of the Kriso container ship. A kernel-based self-parametrisation approach of the design surface is combined with mesh-morphing techniques to drive the 150,000 shape parameters of the vessel without the need to revisit or differentiate the CAD environment during the optimisation. The optimisation process obeys to practical constraints. The optimised vessel displays more than 5% reduction of total drag while maintaining main dimensions and displacement.

## ARTICLE HISTORY

Received 4 September 2017

Accepted 26 November 2017

## KEYWORDS

Sensitivity computation;  
adjoint two-phase flow;  
adjoint volume-of-fluid;  
CAD-free shape optimisation;  
ship hydrodynamics;  
Navier-Stokes simulations

## 1. Introduction

Computational modelling and simulation has matured towards a viable marine engineering design practice. Marine engineering free-surface flow simulations were previously dominated by potential flow methods. While potential flow methods still find their well-appreciated applications, e.g. during the early design or for longer term seakeeping studies, recent interest in accurate simulations of viscous and turbulent effects has motivated the development of many very similar viscous two-phase flow solvers during the last two decades, cf. the overview provided by Larsson et al. (2013). Such viscous two-phase flow simulations are nowadays usually performed with finite volume VoF-procedures for two immiscible, incompressible phases, i.e. air and water (Hirt and Nichols 1981). Virtually all procedures use a compressive approximation for the mixture fraction to keep the discrete interface sharp, e.g. Ubbink (1997), Muzaferija and Perić (1999), Rusche (2002), So et al. (2011) or Waclawczyk and Koronowicz (2008). Moreover, they often employ a pressure correction or pressure projection scheme that is embedded in a segregated solution process (Ferziger and Perić 2002).

Supplementary to the establishment of a simulation-based performance analysis, the industrial needs for design optimisation have subsequently motivated an increased interest in the development of computational optimisation procedures. Computational optimisation methods can be categorised into two different branches, following either global (statistical) zero-order or local (gradient-based) first-order approaches.

The optimisation effort generally scales with both the computational effort associated with the design evaluation procedure and the number of considered optimisation parameters. For zero-order methods, the number of required design evaluations scales nonlinearly with the number of design parameters. This suggests to employ particularly cheap design evaluation methods, e.g. potential flow methods, and a reduced parameter set in conjunction with global optimisation procedures. For direct first-order methods – e.g. Martins et al. (2003) and Newman et al. (2002) – the number of design evaluations required to approximate the gradient of the objective scales linearly with the amount of design parameters. Contrary to this, the effort associated to (indirect) adjoint first-order methods as pioneered by Jameson (1988) and Pironneau (1974), is independent from the amount of design variables, but scales with the amount of objective functions.

Many industrial applications seek for an optimisation – or at least an improvement – of a given design, which features a large number of design parameters, regarding a single or a very small amount of objectives. In such cases, gradient-based (local) optimisation procedures using adjoint systems are deemed the most efficient approach. A prominent example refers to the optimisation of complex shapes, where the required resolution of prominent flow features implies a surface discretisation that often employs  $O(100,000)$  elements which serve as design parameters during the optimisation. Examples for adjoint shape optimisations for

**CONTACT** Jörn Kröger ✉ [joern.kroeger@tuhh.de](mailto:joern.kroeger@tuhh.de) Fluid Dynamics and Ship Theory (M8), Hamburg University of Technology (TUHH), Am Schwarzenberg-Campus 4, D-21073 Hamburg, Germany

\*Present address: Pella Sietas GmbH, Neuenfelder Fährdeich 88, D-21129 Hamburg, Germany

© University of Duisburg-Essen 2018

buildings, aircraft, ships or cars were reported by Jameson (1995), Othmer (2014), Zymaris et al. (2009), Stück et al. (2011), Bletzinger (2014), Papoutsis-Kiachagias et al. (2015) and Kröger and Rung (2015).

### 1.1. Computational shape optimisation using adjoint methods

Two options for deriving the discrete adjoint equations are conceivable, i.e. following the continuous or the discrete adjoint approach (Peter and Dwight 2010). The former derives the adjoint PDE system, often referred to as the ‘dual’ system, in continuous space and subsequently discretises them. The latter exclusively operates in discrete space and formulates the adjoint of the discretised (linearised) governing PDE system, usually referred to as the ‘primal’ system, by transposing the discrete primal operators. It provides the exact derivative of the discrete objective function so that the discrete adjoint consistency is satisfied and convergence of the optimisation is assured. The continuous adjoint method is easier to apply to simulation procedures where the Jacobian matrix or the complete source are unavailable, such as the segregated solvers frequently employed for industrial simulations of incompressible hydrodynamic flows. Moreover, the method inherits the computational efficiency of the primal solver due to the extensive reuse of software modules. The approximation of the continuous adjoint PDE system is a delicate issue. Unless derived with due care, e.g. Liu and Sandu (2005) or Stück and Rung (2013), the resulting approximation might be inconsistent with the transposition of the linearised discrete primal system and the calculated shape derivatives might not exactly agree with the computed derivatives obtained from the primal solver on a finite mesh. The present approach merges aspects of continuous and discrete adjoint methods. In this hybrid adjoint strategy, formerly reported by Stück and Rung (2013), the adjoint PDE is derived and subsequently the approximations of the individual building blocks of the PDE are constructed via summation by parts from the primal discretisation.

Adjoint shape optimisation methods can be performed in a CAD-free or a CAD-based framework. Classical CAD-based strategies considerably reduce the dimension of the design space compared to the number of analysis degrees of freedom (Armstrong et al. 2007). This, however, introduces a restriction of the detectable shape optima, which in turn can significantly reduce the attainable improvements. Another challenge of CAD-based strategies refers to the change of design variables, which requires differentiating the shape with respect to the design parameters. For complex industrial shapes and black-box CAD tools, the differentiation can usually not be performed analytically. Instead, it follows from

less accurate numerical forward differentiations and needs cumbersome updates as the shape evolves (Robinson et al. 2012). The present paper therefore focuses on a CAD-free approach along a route recently been suggested by Bletzinger (2014) and Kröger and Rung (2015).

### 1.2. Utilising adjoint sensitivities for hydrodynamic shape optimisation

Many shape optimisation examples related to ship hydrodynamic applications of adjoint Reynolds-Averaged Navier–Stokes methods (RANS) are restricted to zero Froude number, e.g. optimising the homogeneity of the axial wake, and have previously been published by the authors in Stück et al. (2010b, 2011), Stück (2012), Stück and Rung 2013 or Kröger and Rung (2015). They all refer to shape updates driven by the gradient of an objective functional  $J$ , which in this paper refers to the drag of a vessel. The optimisation aims to successively reduce the objective functional  $J$  or the contribution of specific surface patches  $d\Gamma$  to the objective functional towards a minimum by appropriate changes of the design surface  $\Gamma_D$  in the direction of the surface normal. This change is performed in a steepest descent approach against the direction of the local gradient, i.e.

$$J \rightarrow J - \int_{\Gamma_D} [\Delta n G] d\Gamma \quad (1)$$

The symbol  $G$  denotes to the gradient of the objective functional,  $\Delta n$  refers to the spatial step size which is aligned to the surface-normal vector of the considered surface elements  $d\Gamma$ . For the optimisation procedure employed in this paper, the gradient is derived from the adjoint sensitivities that are efficiently provided by the adjoint solver. Owing to the inherent linearisation of Equation (1), the shape updates need to be small, which restricts the user-specified (constant) step size  $\Delta n$  to sufficiently small values. Typically, we employ a fraction of a main dimension of the optimised object, e.g. an initial absolute step size of 0.02 m for a ship with a length of 200 m.

The peculiarity of adjoint methods is that they allow to determine the gradient of the objective function using the present shape only, i.e. without actually investigating (computing) the modified shape and performing an associated flow simulation. Moreover, the gradient can be computed simultaneously for all modifications, i.e. for all shape parameters, in one single calculation step at virtually the same cost. A ship-technical example, that can highlight the practical benefit of adjoint sensitivity studies to approximate the gradient of the objective, refers to the hull optimisation of a Panamax container vessel. Figure 1 shows the corresponding sensitivity distribution with the aim of drag

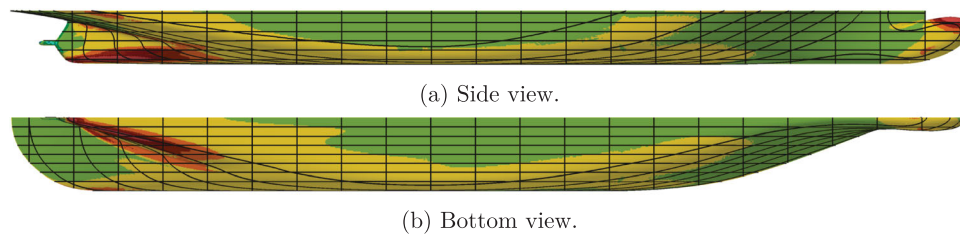


**Figure 1.** Sensitivity contours for a Panmax container vessel with respect to the reduction of the total resistance (single-phase test-case). The resistance is reduced by a local decrease (increase) of the local displacement in regions of positive (negative) sensitivities, i.e. reducing the fullness of the bulbous bow and the lower part of the skeg: (a) side view and (b) bottom view.

reduction along the hull surface, frequently labelled as sensitivity map. The quasi-continuous sensitivity information either can guide the designer during a manual shape optimisation or can be exploited in automatic optimisation procedures. Related to the former it is worth mentioning that one can also discard the suggestion of the sensitivity map in selected regions and usually still improve the design.

The present automatic adjoint optimisation procedure loops a number of design cycles where each cycle inheres: (a) a primal flow analysis for the current shape (i.e. a standard RANS-simulation), (b) a corresponding adjoint analysis to compute the shape sensitivities, (c) the computation of the (smooth) gradient out of the (raw) sensitivity, (d) an update of the current CFD surface mesh based on a given search direction combining the gradient with a prescribed step size and (e) a modification of the volume mesh with the aid of mesh-morphing strategies. The paper at hand covers the adjoint computation of shape sensitivities (b) for two-phase flows. An in-depth discussion of efficient means for the robust and smooth deformation of discrete shapes and the development of an adjoint optimisation process that satisfies non-hydrodynamic (e.g. manufacturing) constraints is given in Kröger and Rung (2015) and Kröger (2016).

If multi-objective optimisation studies are of interest, a combined sensitivity map needs to be computed. The latter can be obtained from a weighted superposition of results from individual adjoint computations or alternatively with one adjoint computation for a combined objective, that is composed from weighted contributions of all considered objectives. Distinct simulations for each objective functional typically provide the designer a deeper insight and in addition support a better understanding of corresponding local contradictions or potentials.

### 1.3. Present contributions

Recent developments of adjoint flow solvers did mainly focus on single-phase solvers. A fairly limited work was devoted to the application of adjoint methods for viscous two-phase flow problems.

Early applications of adjoint methods to the optimisation of two-phase flow problems were based on

potential flow methods. A design framework based on potential theory for the optimisation of surface ships and submarines operating near a free surface was developed by Ragab (2003). Covered objectives included the minimisation of the wave resistance, the optimisation towards a prescribed target pressure distribution and prescribed free surface wave patterns. The adjoint complement to a potential flow solver was developed and applied by Söding (2001a,b,c) to reduce the wave resistance of ships.

An adjoint Euler solver was developed by Soto et al. (2004) to reduce the wave resistance of merchant ships. The free-surface equation was not subject to variation. An adjoint procedure based on a surface-tracking Euler method was used by Martinelli and Jameson (2007) to reduce the wave resistance of a Wigley hull. The development of an adjoint level-set Euler solver was documented by Palacios et al. (2012). The solver is applicable for primal steady-state solutions and was applied to 2D- and 3D-obstacles in free-surface channel-flows. The authors did also present an adjoint level-set RANS solver in Palacios et al. (2013), but applications were restricted to 2D cases. An adjoint VoF-RANS solver was discussed in Springer (2014) and was applied for the adaptation of the running attitude of ships, but neglects many of the adjoint coupling terms. Their main objective functional refers to the equilibrium of the trim moment at steady state. Hence, the computational objective was devoted to finding the roots rather than a minimum of a functional, a weak adjoint coupling was still reasonable as the adjoint consistency was not that important.

The presented work extends an existing segregated adjoint single-phase solver reported in Stück et al. (2011), Stück and Rung (2013) and Stück (2012) to the framework of two-phase flows. The adjoint system is derived via the hybrid adjoint approach. Although the primal flow simulation is performed in the time domain, the intended application focuses on steady-state results. Thus, expensive time-accurate adjoint schemes are not required. Following the frozen turbulence assumption, the variation of turbulence parameters is neglected due to their minor significance in attached pressure dominated hydrodynamic flows, where turbulence and its modelling details are usually

not that crucial. Still, the influence of the shape modification on the turbulent flow quantities is continuously accounted for during the primal flow update performed for each optimisation step. The variation of the flow properties introduces many additional terms that constitute a strong coupling of the adjoint PDE system. Subtle changes of their discrete approximation can significantly impede the accuracy and robustness. Moreover, VoF-methods for immiscible fluids feature a discontinuity of the phase field which makes the discrete treatment in an adjoint framework particularly challenging. These challenges have motivated the restriction of previous work to either reduced (Springer 2014), level-set based (Palacios et al. 2012, 2013) or diffusive interface schemes (Garcke et al. 2016). Different from Springer (2014), the presented approach considers all adjoint coupling terms in conjunction with sharp interface VoF-schemes, and reports on strategies to stabilise the adjoint procedure. With regard to more simplified adjoint schemes, the significance of individual adjoint coupling terms for the attainable predictive accuracy of shape sensitivities is investigated.

The remainder of the paper is organised as follows: The numerical framework and the governing equations are described in Section 2. The section also reports on the derivation of the adjoint two-phase solver. Section 3 is concerned with verification and validation studies. Applications to a container vessel are displayed in Section 4. Final conclusions are drawn in Section 5. Throughout this paper, vectors and tensors are defined by reference to cartesian coordinates. Einstein's summation convention is used over repeated lower case latin indices.

## 2. Mathematical framework

### 2.1. Primal two-phase flow method

#### 2.1.1. Governing equations

The numerical solution of the primal RANS equations constitutes the basis for the simulation method. Using the Boussinesq-viscosity hypothesis to model turbulence, the incompressible, unsteady RANS equations in residual formulation read

$$R_i : \rho \frac{\partial u_i}{\partial t} + \rho u_k \frac{\partial u_i}{\partial x_k} - \frac{\partial}{\partial x_k} (2\mu_{\text{eff}} S_{ik} - p \delta_{ik}) \quad (2)$$

$$- \rho g_i - f_i = 0$$

$$Q : - \frac{\partial u_i}{\partial x_i} = 0 \quad (3)$$

where  $u_i$  refers to the cartesian coordinates of the mean velocity, whereas  $p$  and  $\rho$  denote the pressure and the fluid density, respectively. The coordinates of the unity and the strain rate tensors refer to  $\delta_{ik}$  and  $S_{ik}$ , respectively. Body forces distinguish between gravity-

related contributions, e.g.  $g_i = -9.81 \text{ m/s}^2 \delta_{i3}$ , and other contributions ( $f_i$ ). The effective viscosity  $\mu_{\text{eff}} = \mu + \mu_T$  constitutes the sum of the molecular and the turbulent viscosity. In the present study, the turbulent viscosity is modelled by an SST  $k$ - $\omega$  two-equation model (cf. Menter et al. 2003). For industrial two-phase flow simulations, the VoF-method constitutes a standard due to its versatility, the inherent conservation of mass and the robustness against changes of interface topology. The method aims to capture the volumetric concentration  $c$  of a foreground fluid phase. For immiscible fluids, the material state will be conserved, i.e. the concentration is invariable, which yields

$$C : \frac{Dc}{Dt} = \frac{\partial c}{\partial t} + u_k \frac{\partial c}{\partial x_k} = 0 \quad (4)$$

Local material properties are calculated from a simple equation of state for incompressible/constant viscosity fluid phases using the concentration  $c$ , e.g.

$$\rho = c\rho_a + (1 - c)\rho_b, \quad \mu = c\mu_a + (1 - c)\mu_b \quad (5)$$

Fluid  $a$  is denoted as *foreground fluid* and fluid  $b$  as *background fluid*. The present study assigns  $c = 1$  to the foreground phase (i.e. air) and  $c = 0$  to the background phase (i.e. water). Physically, the concentration value is restricted to  $c = 0$  and  $c = 1$ . Intermediate values might occur during the numerical simulation and denote the position of the free surface. They are usually suppressed by the compressive approximation of the convection of  $c$  to keep the interface sharp. The computation of spatial concentration gradients can pose a challenge due to the jump of the concentration  $c$  for immiscible flows.

The adjoint solution points backward in time and is linearised around the current primal flow solution. Thus, the attractiveness of adjoint methods reduces for the optimisation of unsteady flows, due to memory requirements to record the complete time history of the primal problem. Formally, the present problem is performed in time domain. However, although the solution procedure is unsteady, we are seeking for the steady-state wave field and the related drag. Hence, robust convergence based upon plausible – i.e. physically realizable solutions – but not time accuracy is required from the primal and the dual intermediate flow fields that represent the solution process towards the final, quasi-steady solution. Thus, the adjoint solution can be computed solely from the converged, quasi-steady primal flow field.

#### 2.1.2. Numerical procedure

The finite-volume Navier–Stokes procedure FreSCo<sup>+</sup> (Rung et al. 2009) constitutes the basis for the present development. The segregated algorithm is based on the strong conservation form of the momentum equations and employs a cell-centred, collocated



storage arrangement for all transport properties. Unstructured overset grids of arbitrarily shaped polyhedral cells can be used (Völkner et al. 2017). The implicit numerical approximation is second-order accurate in space and time. A SIMPLE pressure correction scheme is employed to determine the pressure for incompressible or compressible (cavitating) flows (Yakubov et al. 2015). Various statistical (RANS) or scale-resolving (DES, LES) turbulence-modelling strategies are available. Parallelisation follows a domain decomposition approach which scales down to about 15,000 cells per process (Yakubov et al. 2013). Applications of the employed procedure to marine engineering flows are reported in Luo-Theilen and Rung (2017) among other publications.

## 2.2. Adjoint two-phase flow method

For the development of the adjoint method, the design problem is regarded as a control problem. The starting point of the method is an augmented objective functional that combines the actual objective(s) with the governing flow equations ( $R_i$ ,  $Q$ ,  $C$ ). Applying a variational calculus to the augmented objective functional introduces a (geometric) variation to the control, i.e. for the presented approach a variation to the position of the boundary patches of the CFD grid along their local boundary normal vector. The variation of the control yields variations of the flow field variables ( $u_i$ ,  $p$ ,  $c$ ) and subsequently the objective functional  $J$ , herein the drag of a ship. The linearised response of the objective functional to variations of the control constitutes the *sensitivities*, i.e. a discrete version of the gradient of the objective functional with respect to the control ( $G$  in Equation (1)). Thus, the primal flow field constitutes the link between the objective and the control and a variation is deemed admissible if it is associated with a valid solution of the primal system. Therefore, the primal system is considered as a constraint to the control problem.

### 2.2.1. Augmented objective functional

By reference to the Lagrangian method, the objective functional  $J$  is combined with the residual form of the governing Equations (2)–(4) to obtain an augmented objective functional  $L$ , namely

$$L = \int_{\Gamma_o} j_\Gamma d\Gamma + \int_{\Omega_o} j_\Omega d\Omega \quad (6)$$

$$+ \int_{\Omega} d\Omega \left\{ \hat{u}_i \left[ \rho \frac{\partial u_i}{\partial t} + \rho u_k \frac{\partial u_i}{\partial x_k} \right. \right. \quad (7)$$

$$+ \frac{\partial}{\partial x_k} \left\{ p \delta_{ik} - \mu \left( \frac{\partial u_i}{\partial x_k} + \frac{\partial u_k}{\partial x_i} \right) \right\} - \rho g_i \right\} - \hat{p} \left[ \frac{\partial u_i}{\partial x_i} \right] + \hat{c} \left[ \frac{\partial c}{\partial t} + u_k \frac{\partial c}{\partial x_k} \right] \quad (8)$$

where  $j_\Gamma$  and  $j_\Omega$  denote the surface and volume specific contributions to the objective  $J$ , respectively. The residuals of the governing equations serve as constraints. The Lagrangian multipliers  $\hat{u}_i$ ,  $\hat{p}$  and  $\hat{c}$  constitute the adjoint or dual field variables and are employed as weights to the constraints.

The derivation of the adjoint system follows from linear variations of the Lagrangian  $L$  with respect to the control and the primal state variables ( $u_i$ ,  $p$ ,  $c$ ). The method aims to avoid the numerical effort associated with the re-evaluation of the primal flow field for each control variation using appropriately chosen adjoint variables, which follow from the solution of the adjoint PDE system. This allows one to evaluate the (linear) response of the objective functional on variations of the control independent of the flow field variation.

For the considered quasi-steady flow problems, the augmented objective functional is evaluated (i.e. the adjoint analysis is performed) at a primal solution time  $t_{steady}$ , for which the time derivatives that contribute to the numerical procedure chosen for the solution of the volume-of-fluid framework have practically vanished.

The adjoint system depends on the objective functional  $J$ . In the present study, a boundary-based hydrodynamic force objective functional is declared over the surface of the design object ( $\Gamma_o = \Gamma_D$ ). This constitutes the sum of shear and pressure forces along  $\Gamma_o$ , which is projected into a particular direction  $d_i$  (e.g. the direction of the heading)

$$J_\Gamma = \int_{\Gamma_o} j_\Gamma d\Gamma = \int_{\Gamma_o} (pn_i - 2\mu S_{ik}n_k) d_i d\Gamma \quad (9)$$

In general, the design surface  $\Gamma_D$  does not need to agree with the location of the objective functional. Optionally, the extent of the surface that is addressed for the evaluation of the objective functional can be restricted to a specific part of the flow exposed geometry. For the practical application case presented in this paper, the entire hull of a ship except the deck is considered for the evaluation of the objective functional.

### 2.2.2. Variational form of the augmented objective functional

In shape optimisation, the design surface is subjected to variations, i.e. position changes in the surface-normal direction. However, the variation of  $L$  comprises further contributions. A linear expansion yields (a) *local variations*  $L'$  of the flow properties at the old position, (b) *convective variations*  $L^c$  related to a position change within the old flow field and (c) *geometric variations*  $L^g$  due to the change of geometric properties, i.e.  $\tilde{L} = L' + L^c + L^g$ . Along the design boundaries, all contributions have to be

considered. Along the remaining boundaries and in the interior domain, the state is only exposed to local variations. In the following, the notation  $\phi'$  represents the *local* variation of a quantity  $\phi$ . The same holds for the term *variation* if not indicated in a different way.

The present variation of state variables comprises  $u'_i$ ,  $p'$ ,  $\rho' = c'(\rho_a - \rho_b) = c'\rho_\Delta$  and  $\mu' = c'(\mu_a - \mu_b) = c'\mu_\Delta$ . Turbulence parameters are not subject to variations. This is a common approach employed by many authors that look at practical flows due to the minor importance of the adjoint turbulence model. The approach is particularly defensible in flows governed by hydrostatic pressure contributions. All turbulence model parameters are of course continuously updated during the primal state evaluation of each design cycle.

### 2.2.3. Continuous adjoint equation system

The derivation of the adjoint PDE system is straightforward but quite lengthy. For the sake of brevity, the paper is restricted to an illustrative example. Further details are omitted and the interested reader is referred to the Ph.D. works of Stück (2012) and Kröger (2016) for a comprehensive derivation.

As regards the simple example of a generic convective term, this linear variational framework yields

$$\int_{\Omega} \hat{\phi} \left( \rho u_k \frac{\partial \phi}{\partial x_k} \right)' \rightarrow \int_{\Omega} \hat{\phi} \left( \rho' u_k \frac{\partial \phi}{\partial x_k} + \rho u'_k \frac{\partial \phi}{\partial x_k} + \rho u_k \frac{\partial \phi'}{\partial x_k} \right) \quad (10)$$

The variational form is subjected to integration by parts that shifts derivatives from the variation of state variables to the adjoint variables.

$$\begin{aligned} & \int_{\Omega} \hat{\phi} \left( \rho' u_k \frac{\partial \phi}{\partial x_k} + \rho u'_k \frac{\partial \phi}{\partial x_k} + \rho u_k \frac{\partial \phi'}{\partial x_k} \right) \\ &= \int_{\Omega} \left[ \rho' \left( u_k \hat{\phi} \frac{\partial \phi}{\partial x_k} \right) + u'_k \left( \rho \hat{\phi} \frac{\partial \phi}{\partial x_k} \right) \right] \\ &+ \int_{\Gamma_o} \phi' \rho u_k \hat{\phi} - \int_{\Omega} \phi' \left[ \frac{\partial (\rho u_k \hat{\phi})}{\partial x_k} \right] \end{aligned} \quad (11)$$

Moreover, we use an optional supplementary integration to avoid the differentiation of the primal concentration across the free surface. The first two terms are advective contributions, which couple the adjoint momentum and adjoint concentration with the adjoint  $\hat{\phi}$ -equation. Finally, the variational Lagrangian  $\tilde{L}$  can be rearranged as follows:

$$\begin{aligned} \tilde{L} = & \int_{\Gamma} \{ u'_i (\rho \hat{u}_i u_k + 2\mu \hat{S}_{ik} - \hat{p} \delta_{ik} + \hat{c} c \delta_{ik}) \\ & - \hat{u}_i 2\mu S'_{ik} + p' \delta_{ik} \hat{u}_i + c' (\hat{c} u_k - \hat{u}_i \mu_\Delta 2S_{ik}) \} d\Gamma_k \end{aligned} \quad (12)$$

$$+ \int_{\Omega} \left\{ u'_i \left( -\rho \frac{\partial \hat{u}_i}{\partial t} + \rho \hat{u}_k \frac{\partial u_k}{\partial x_i} - \rho u_k \frac{\partial \hat{u}_i}{\partial x_k} \right) - \frac{\partial}{\partial x_k} [2\mu \hat{S}_{ik} - \hat{p} \delta_{ik}] - c \frac{\partial \hat{c}}{\partial x_i} \right\} \quad (13)$$

$$- p' \left( \frac{\partial \hat{u}_i}{\partial x_i} \right) + c' \left( -\frac{\partial \hat{c}}{\partial t} - u_k \frac{\partial \hat{c}}{\partial x_k} + \rho_\Delta \hat{u}_i u_k \frac{\partial u_i}{\partial x_k} + \mu_\Delta 2S_{ik} \frac{\partial \hat{u}_i}{\partial x_k} - \hat{u}_i \rho_\Delta g_i \right) \} d\Omega \quad (14)$$

$$+ \int_{\Gamma_o} \tilde{j}_\Gamma d\Gamma + \int_{\Omega} j'_\Omega d\Omega \quad (15)$$

The volume integral immediately yields the adjoint field equations, which are solved to allow for arbitrary admissible local variations of the flow field, namely

$$\hat{R}_i : -\rho \frac{\partial \hat{u}_i}{\partial t} - \underbrace{\rho u_k \frac{\partial \hat{u}_i}{\partial x_k}}_{\text{CONV}_{R_i}^{\phi'}} = - \underbrace{\rho \hat{u}_k \frac{\partial u_k}{\partial x_i}}_{\text{ADV}_{R_i}^{\mu'}} \quad (16)$$

$$+ \underbrace{c \frac{\partial \hat{c}}{\partial x_i}}_{\text{ADV}_C^{\mu'}} + \frac{\partial}{\partial x_k} \left( \underbrace{2\mu \hat{S}_{ik}}_{\text{DIFF}_{R_i}^{\mu'}} - \hat{p} \delta_{ik} \right) - \frac{\partial j_\Omega}{\partial u_i}$$

$$\begin{aligned} \hat{C} : & -\frac{\partial \hat{c}}{\partial t} - \underbrace{u_k \frac{\partial \hat{c}}{\partial x_k}}_{\text{CONV}_C^{\phi'}} = - \underbrace{\rho_\Delta \hat{u}_i u_k \frac{\partial u_i}{\partial x_k}}_{\text{ADV}_{R_i}^{\rho'}} - \underbrace{\mu_\Delta 2S_{ik} \frac{\partial \hat{u}_i}{\partial x_k}}_{\text{DIFF}_{R_i}^{\mu'}} \\ & + \underbrace{\hat{u}_i \rho_\Delta g_i}_{\text{HYDR}_{R_i}^{\rho'}} - \frac{\partial j_\Omega}{\partial c} \end{aligned} \quad (17)$$

$$\hat{Q} : \frac{\partial \hat{u}_i}{\partial x_i} = \frac{\partial j_\Omega}{\partial p} \quad (18)$$

The unsteady terms require integration by parts with respect to time. In conclusion, the adjoint evaluation for an unsteady primal simulation sweeps backwards from the final to the very first time step. As outlined before, the current work focuses on quasi-steady primal flows. Hence, for the converged primal solution the unsteady term vanishes and the time history is meaningless. All adjoint time steps are linearised around the same converged primal flow field. Moreover, the transient terms (16) and (17) are only optionally included to strengthen the adjoint equation system and vanish for the converged adjoint solution.

To outline the primal origin of the respective terms, they are underbraced. The advective terms  $\text{ADV}_{R_i}^{\rho'}$  and  $\text{ADV}_{R_i}^{\mu'}$  originate from the *primal momentum equation*  $R_i$  and contribute to the adjoint concentration and momentum equation. The terms  $\text{CONV}_{R_i}^{\phi'}$  and  $\text{CONV}_C^{\phi'}$  come from the convective term of the primal momentum and concentration balance and contribute

to their adjoint complements. The terms  $DIFF_{R_i}^{u'}$  and  $DIFF_{R_i}^{u''}$  originate from the diffusion terms in the primal momentum equations and contribute to the adjoint momentum and concentration equation. Another term denotes the contribution from the buoyancy variation to the adjoint concentration equation ( $HYDR_{R_i}^{p'}$ ).

#### 2.2.4. Variation of the objective functional

The variation of the hydrodynamic force criterion (9) comprises local, convective and geometric terms. Validation studies conducted by Stück (2012) show that the geometric variation is of minor importance for the predictive accuracy of the sensitivities and can be neglected ( $J_\Gamma^g = 0$ ). The local variation reads

$$J_\Gamma^l = \int_{\Gamma_o} (p'n_i - 2c'\mu_\Delta S_{ik}n_k - 2\mu S'_{ik}n_k)d_i d\Gamma \quad (19)$$

The convective variation  $J_\Gamma^c$  accounts for the variation of the objective due to the position change of the surface in the previous flow field. In the absence of hydrostatics, the convective variation vanishes when curvature terms are neglected since  $\partial\tau^{nt}/\partial n = \partial p/\partial n = 0$ . In flows that experience a hydrostatic pressure contribution, the pressure gradient in the surface-normal direction reads  $\partial p/\partial n = n_k(\partial p/\partial x_k) = \rho g_k n_k$ . Thus, the convective variation  $J_\Gamma^c$  with respect to a surface-normal perturbation  $\Delta n = \Delta x_j n_j$  reads

$$\begin{aligned} J_\Gamma^c &= \int_{\Gamma_o} \Delta n \frac{\partial J_\Gamma}{\partial n} d\Gamma = \int_{\Gamma_o} \Delta n \left( n_i \frac{\partial p}{\partial n} \right) d_i d\Gamma \\ &= \int_{\Gamma_o} \Delta n (n_i \rho g_k n_k) d_i d\Gamma \end{aligned} \quad (20)$$

#### 2.2.5. Adjoint boundary terms

To derive boundary conditions for the adjoint variables, the boundary terms of the Lagrangian are analysed under consideration of the primal boundary conditions and contributions from a boundary-based objective functional in continuous and discrete space, i.e. for the perturbed discrete balances of the primal flow in the boundary control volumes. Table 1 summarises the adjoint boundary conditions for the adjoint two-phase flow. The derivation follows the strategy pursued to derive boundary conditions for the adjoint single-phase problem (cf. Othmer 2008; Stück 2012). The detailed discussion of the derivation of boundary conditions for the adjoint two-phase flow problem is given in Kröger (2016). In the following, special emphasis is given to the derivation of the sensitivity equation.

Wall boundaries that coincide with parts of the design surface ( $\Gamma \subset \Gamma_D$ ) require special attention. Both the local variation and the convective variation due to a surface-normal perturbation  $\Delta n = \Delta x_k n_k$  of the design shape  $\Gamma_D$  have to be considered. In the

primal system, a Dirichlet condition for the primal velocity ( $u_i = 0$ ) is used. A Neumann condition is imposed for both the primal pressure and the primal concentration. The remaining boundary terms are

$$\tilde{L} = \int_{\Gamma_o} \{ (p'\delta_{ik} - 2c'\mu_\Delta S_{ik} - 2\mu S'_{ik})(\hat{u}_i + d_i) \quad (21)$$

$$+ u'_i(2\mu\hat{S}_{ik} - \hat{p}\delta_{ik} + \hat{c}c\delta_{ik}) \quad (22)$$

$$+ \Delta x_k(\rho g_j n_j) n_i d_i \} d\Gamma_k \quad (23)$$

If the hydrodynamic force objective is evaluated on the design surface, Equation (21) yields the adjoint boundary condition  $\hat{u}_i = -d_i$  for the adjoint momentum. The boundary condition is  $\hat{u}_i = 0$  if no force objective is active on the design surface. The convective variation of the objective functional (23) directly contributes to the sensitivity equation. This term is governed by the primal hydrostatic pressure gradient in the surface-normal direction ( $\rho g_j n_j$ ). Interestingly, it is independent of adjoint quantities and constitutes a simple additional sensitivity contribution. The local variation (22) is reformulated by virtue of the linear expansion of the primal no-slip condition  $u'_i = -\Delta n(\partial u_i/\partial n)$  to obtain the contribution to the sensitivity equation:

$$\int_{\Gamma_o} u'_i(2\mu\hat{S}_{ik} - \hat{p}\delta_{ik} + \hat{c}c\delta_{ik})d\Gamma_k \quad (24)$$

$$= \int_{\Gamma_o} -\Delta n \frac{\partial u_i}{\partial n} (2\mu\hat{S}_{ik} - \hat{p}\delta_{ik} + \hat{c}c\delta_{ik})d\Gamma_k$$

$$= \int_{\Gamma_o} -\Delta n \left( \mu \left[ \frac{\partial \hat{u}_n}{\partial x_i} + \frac{\partial \hat{u}_i}{\partial x_n} \right] \frac{\partial u_i}{\partial n} - \frac{\partial u_n}{\partial n} (\hat{p} + \hat{c}c) \right) d\Gamma \quad (25)$$

Equation (25) is simplified by exploiting  $\partial u_n/\partial n = 0$  and again neglecting curvature terms. Subsequently, the sensitivity related to the force objective in hydrostatic conditions is obtained from

$$\tilde{L} = \int_{\Gamma_o} -\Delta n \left( \mu \frac{\partial \hat{u}_t}{\partial n} \frac{\partial u_t}{\partial n} - (\rho g_j n_j) n_i d_i \right) d\Gamma \quad (26)$$

**Table 1.** Boundary conditions for adjoint two-phase flow system.

	$\hat{u}_i$	$\hat{p}$	$\hat{c}$
Inlet	$\hat{u}_i = 0$	$\frac{\partial \hat{p}}{\partial x_n} = 0$	$\frac{\partial \hat{c}}{\partial x_n} = 0$
Symmetry	$\hat{u}_n = \frac{\partial \hat{u}_t}{\partial x_n} = 0$	$\frac{\partial \hat{p}}{\partial x_n} = 0$	$\frac{\partial \hat{c}}{\partial x_n} = 0$
Pressure outlet	$\hat{p}n_i = \rho \hat{u}_i u_n + \mu \frac{\partial \hat{u}_i}{\partial x_n} + \hat{c}c n_i$	$\hat{c} = \frac{1}{u_n} \hat{u}_i \mu_\Delta \frac{\partial u_n}{\partial x_i}$	
Wall $\Gamma \setminus \Gamma_o$	$\hat{u}_i = 0$	$\frac{\partial \hat{p}}{\partial x_n} = 0$	$\frac{\partial \hat{c}}{\partial x_n} = 0$
Wall $\Gamma \subset \Gamma_o$	$\hat{u}_i = -d_i$	$\frac{\partial \hat{p}}{\partial x_n} = 0$	$\frac{\partial \hat{c}}{\partial x_n} = 0$

### 2.3. Adjoint discretisation

This section briefly describes aspects about the discretisation of the adjoint PDE within a finite-volume framework based upon a cell-centred, collocated variable arrangement.

The majority of contributions in Equations (16)–(18) are discretised as explicit, second-order accurate source terms. They constitute a strong coupling in the segregated solver. As opposed to this, the convective and diffusive fluxes as well as the optional transient terms are implicitly discretised.

The flux approximation starts from the discrete primal fluxes. Their contribution to the discrete variational form of the Lagrangian is obtained by augmenting the linearised discrete flux variation with the cell-specific adjoint variable. We confine ourselves again to the example of convective kinematics in conjunction with first-order upwind differencing (UDS) of the primal and refer to Stück and Rung (2013) for more details. For the sum of all control volumes ( $P$ ) and faces ( $f$ ), the discrete contribution of the primal convection to  $L$  reads

$$\sum_P \hat{\phi}_P \sum_{f(P)} (\dot{m}^f \phi^f) = \sum_P \hat{\phi}_P \sum_{f(P)} (\rho U_k \Delta \Gamma_k)^f \phi^f \quad (27)$$

The respective linearised variational contribution yields an advective and a convective term

$$\sum_P \hat{\phi}_P \sum_{f(P)} (\dot{m}^f \phi^f)' = \sum_P \hat{\phi}_P \sum_{f(P)} [(\rho U_k \Delta \Gamma_k)^f \phi^f + \dot{m}^f \phi'^f] \quad (28)$$

Using UDS for the primal face values in Equation (28), the variation is approximated accordingly

$$\sum_P \hat{\phi}_P \sum_{f(P)} [\max(\dot{m}^f, 0) \phi'_P - \max(-\dot{m}^f, 0) \phi'_N] \quad (29)$$

Similar to the continuous approach, namely Equation (11), local variations of flow variables are factored out to determine the sensitivity independent of the state derivative. While the reformulation of the continuous Lagrangian employs *integration-by-parts*, reformulating the discrete Lagrangian utilises *summation-by-parts* (cf. Nadarajah 2003; Stück 2012). For the considered example in Equation (29), one converts the double sum into a global sum over all faces. Since each adjoint contribution occurs twice – once for the left ( $P$ ) and the right ( $N$ ) control volume – we arrive at

$$\sum_f (\hat{\phi}_P - \hat{\phi}_N) \times [\max(\dot{m}^f, 0) \phi'_P - \max(-\dot{m}^f, 0) \phi'_N] \quad (30)$$

Using continuity arguments, i.e.  $\sum_f \max(\dot{m}^f, 0) = \sum_f \max(-\dot{m}^f, 0)$ , Equation (30) can be rearranged into a downwind differencing scheme

(DDS)

$$\sum_f (\phi'_P - \phi'_N) \times [\max(-\dot{m}^f, 0) \hat{\phi}_P - \max(\dot{m}^f, 0) \hat{\phi}_N] \quad (31)$$

The approach also provides information on the appropriate treatment of the advective fluxes (first term in Equation (28)) as outlined by Stück and Rung (2013). High-order convection approximations of the primal – e.g. the QUICK scheme of Leonard (1991) and their monotonicity-preserving variants, e.g. the TVD-MUSCL approach (van Leer 1979) – are often employed using a compact, one-dimensional deferred-correction approach. The derivation of an adjoint complement from summation-by-parts simplifies substantially when complex non-linear aspects, e.g. with respect to limiter functions, are kept frozen during the variation. As outlined by Stück and Rung (2013), the result usually yields apparently simple ‘mirrored’ discretisation practices. Similar to the approximation of the primal, the adjoint complement is subsequently casted into an implicit baseline DDS and an explicit deferred-correction term.

Diffusion is a self-adjoint process. Hence, central differences are used for both primal and adjoint diffusion fluxes. The transient term is only used to advance the simulation towards a steady state and is approximated with first-order implicit Euler schemes in the primal and the reversed companion in the dual solution process.

#### Adjoint convective concentration transport

The non-dimensional adjoint concentration Equation (32) reveals substantial differences to the primal concentration Equation (4) due to the three contributions from the momentum equations. Using an asterisk to indicate the non-dimensional quantities – e.g.  $u_k = u_k^* V$ ,  $x_k = x_k^* L$ ,  $\hat{c} = \hat{c}^* \hat{C}$ , etc. – in conjunction with a non-dimensional adjoint velocity, the adjoint concentration equation displays Reynolds- and Froude-number expressions in addition to an adjoint production term which resembles a turbulent production term

$$\begin{aligned} & -\frac{L}{VT} \frac{\partial \hat{c}^*}{\partial t^*} - u_k^* \frac{\partial \hat{c}^*}{\partial x_k^*} \\ & = \frac{\rho_\Delta V}{\hat{C}} \left[ -\hat{u}_i u_k^* \frac{\partial u_i^*}{\partial x_k^*} - \left( \frac{\mu_\Delta}{\rho_\Delta VL} \right) 2S_{ik}^* \frac{\partial \hat{u}_i}{\partial x_k^*} + \left( \frac{Lg}{V^2} \right) \hat{u}_i g_i^* \right] \end{aligned} \quad (32)$$

For hydrostatic conditions ( $V \rightarrow 0$ ), a dominance of the Froude-term (last RHS term in Equation (32)) is seen. For non-hydrostatic conditions, the balance reveals similarities to the primal momentum balance.

Owing to the strength of the RHS terms, the approximation focus is shifted from the convective



term to the source terms. Moreover, a compressive approximation dedicated to support a sharp interface seems pointless. It is thus defensible to employ a simplified, robust approximation of the convective term of the adjoint concentration, i.e. an implicit DDS approach which is applied throughout the paper. A similar approach was pursued for the adjoint based design of shock mitigating devices, cf. Stück et al. (2010a). The reduced order of this term may introduce inaccuracies to the adjoint sensitivities. In the present study, the impact on the optimisation remains small as outlined in Section 3.

## 2.4. Numerical procedure

The finite-volume procedure (FreSCo<sup>+</sup>) employs the same infrastructure for the solution of the adjoint and the primal system. This comprises modules for generic field operations (i.e. the calculation of spatial gradients, providing the mesh topology and geometry information, interfaces for parallel communication), for data I/O as well as interfaces to external libraries that provide preconditioners and solvers besides means for domain decomposition and parallelisation. The routines that assemble generic operators, e.g. convection, diffusion and transient terms, are reused for the implementation of the adjoint two-phase solver. Further details are discussed in Stück (2012) and Kröger (2016).

## 3. Verification and validation for a 2D bump in channel

In this section, results from the adjoint two-phase flow solver are compared with results from a corresponding second-order accurate finite-difference study. The considered objective functionals refer to the drag ( $x$ -) and the lift ( $y$ -) forces. The investigated case refers to the flow over a smooth 2D bump embedded into the lower wall of a 2D channel. The shape of the object is inspired by Rumsey (2014) and illustrated in Figure 2. The bump height is described by

$$y = h \left[ \sin \left( \frac{\pi x}{0.9} - \frac{\pi}{3} \right) \right]^4 \quad (33)$$

for  $0.3 \text{ m} \leq x \leq 1.2 \text{ m}$

The height of the channel is assigned to  $H = 3.0 \text{ m}$ . The length and crest height of the obstacle are assigned to

$L = 0.3 \times H = 0.9 \text{ m}$  and  $h = L/12 = H/40 = 0.075 \text{ m}$ . The crest is located at  $x = 0.75 \text{ m}$ .

All simulations refer to laminar flow at a channel Reynolds number of  $Re = HU_b/\nu = 750$ , where  $U_b$  denotes the bulk velocity. Laminar flow conditions are chosen to omit possible inaccuracies introduced by the frozen turbulence approach. Both single-phase and two-phase simulations are performed. Two-phase flow simulations employ a density and viscosity ratio of 830 and 55, respectively.

The inlet of the computational domain is located at  $x = -7.0 \text{ m}$ . The outlet is located at  $x = 7.0 \text{ m}$  and assigned to a prescribed pressure. The distance of both, the inlet and the outlet from the bump exceeds 75 obstacle heights. A no-slip condition is used along the bottom wall of the channel and the bump. The top wall of the channel is assigned to a slip-wall condition. A velocity profile with a boundary-layer thickness of  $0.2 \text{ m}$  was employed at the inlet.

The computational domain is discretised by a structured body-fitted mesh as depicted in Figure 3. Two different configurations are investigated: a domain that considers the free surface in close proximity to the design object (approx. 60,000 cells) and a domain that is extended in the vertical direction to simulate a deeply submerged setup (approx. 70,000 cells). For both configurations, the discretisation of the bump and the free-surface region is identical and resolved by 160 equidistant surface elements (i.e. design faces). The near-wall spacing reads  $5.6 \cdot 10^{-3} L$  in the tangential and  $6.7 \cdot 10^{-5} L$  in the normal direction. The vertical refinement of the free surface region employs the same spacing as the near-wall refinement. Specific attention is subsequently devoted to the faces around the crest (face-IDs 30–130).

### 3.1. Single-phase simulations

This subsection is concerned with adjoint single-phase simulations and corresponding finite-difference (FD) studies. For both primal and adjoint simulations, monotonicity-preserving high-order convection schemes are employed. For the single-phase simulations, hydrostatic effects are neglected. The computed adjoint and FD-sensitivities are compared with each other as well as against results of subsequent two-phase flow simulations performed for identical phase properties. Figure 4 shows the predicted streamlines and pressure contours in the vicinity of the bump.

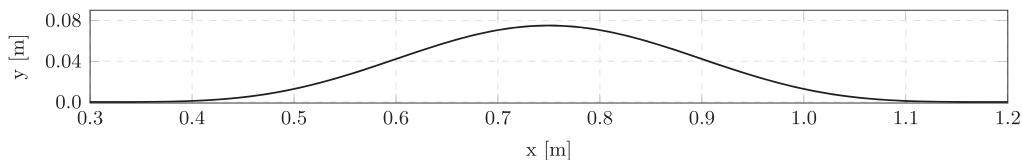
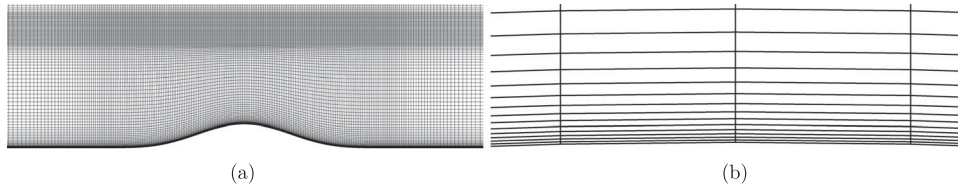
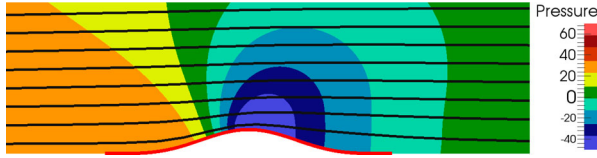


Figure 2. Design object for the 2D bump-in-channel case.



**Figure 3.** Computational mesh employed for the 2D bump-in-channel case: (a) mesh detail with free surface refinement and (b) near-wall mesh detail at the crest.



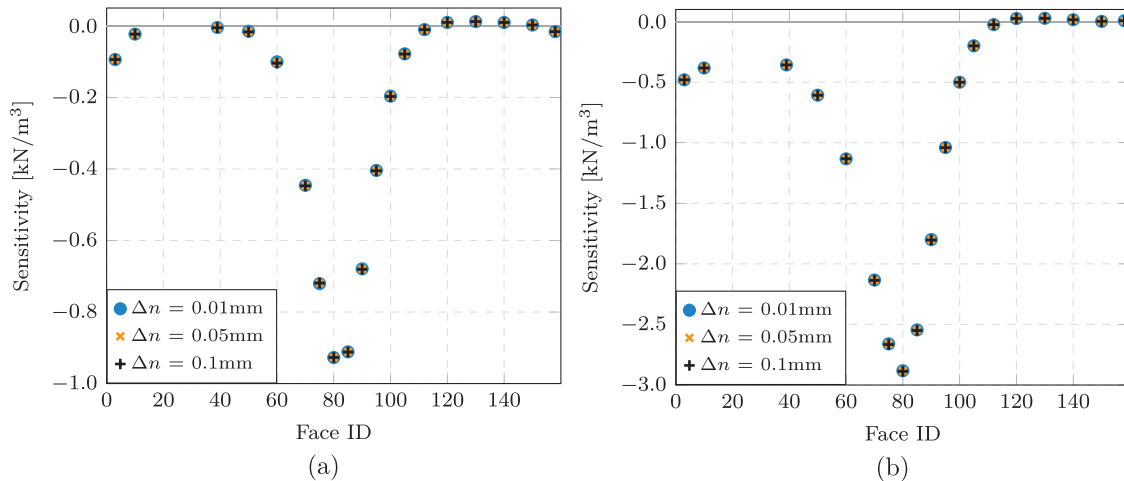
**Figure 4.** Predicted streamlines and pressure contours (Pa) in the vicinity of the design object for a single-phase flow over a bump in a channel.

Direct sensitivities for both objective functionals are determined by finite-differencing. Second-order accurate sensitivities – i.e.  $(J^+ - J^-)/(2\Delta n)$  – are obtained from two additional computations for a small positive and negative surface-normal displacement  $\pm \Delta n$  of each surface element. To restrict the numerical effort, only 19 surface elements are considered. Thus, 38 CFD computations are performed to obtain the sensitivities. The displacement is confined to the target face and its direct neighbours. The complete target face is displaced in the normal direction and the neighbouring faces connect the respective ends of the displaced target face to the remainder of the design surface. The displacement of the volume mesh is realised by a Laplacian mesh deformation procedure, which transfers the boundary deformation into the interior (Kröger and Rung 2015). The associated diffusion coefficient is related to the recursive distance from the design face to confine the mesh deformation to the direct neighbourhood of the perturbed boundary faces.

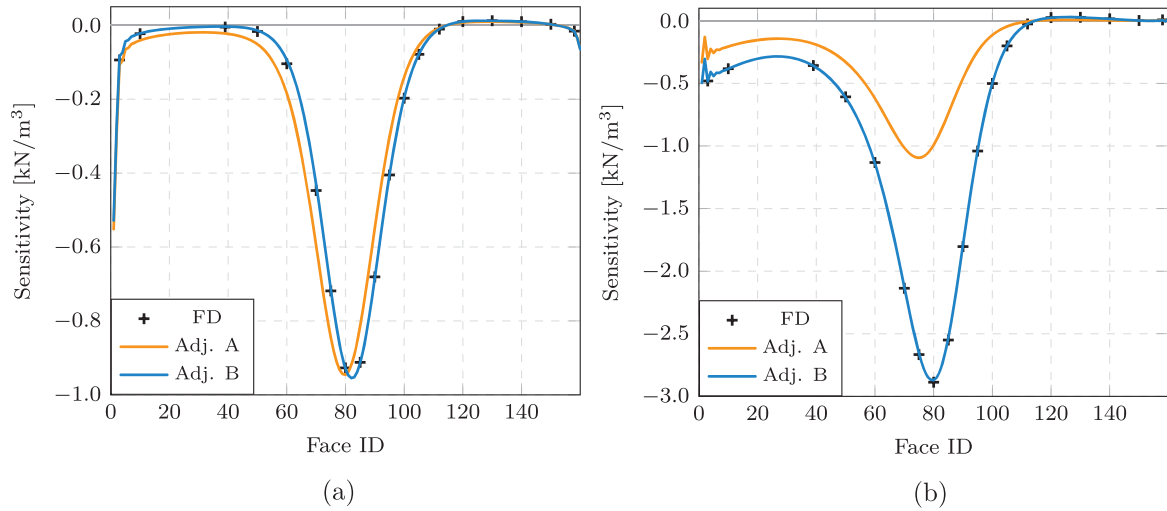
The selection of the step size  $\Delta n$  of the FD study requires attention. The response to the imposed displacement should be confined and must obey the linearity assumption. Moreover,  $\Delta n$  has to be sufficiently large to result in an accurate response and avoid numerical artefacts. A systematic study of various displacement magnitudes was conducted prior to the verification. Figure 5 shows the response of the objective functionals using three different displacement steps  $\Delta n$ ,  $\Delta n/2$  and  $\Delta n/10$  for all selected design faces. It appears that the FD sensitivity is virtually identical for all three step sizes, indicating that all the investigated step sizes lie within a valid range.

Figure 6 compares the result of the direct sensitivity study with the result of adjoint Navier–Stokes simulations for both objective functionals. Neglecting the advection term leads to significant deviations for the sensitivities of the lift, for the sensitivities of the drag a phase shift is observed. Including the advection term leads to a remarkable predictive agreement between the direct and the adjoint sensitivities. Note that the oscillations of the adjoint sensitivities that occur in the vicinity of the upstream and the downstream end of the design surface are caused by the abrupt jump from  $\hat{u}_i = -d_i$  to  $\hat{u}_i = 0$  in the adjoint momentum boundary condition.

This section focusses on the comparison of sensitivities obtained from second-order finite-difference studies with non-regularised, ‘raw’ adjoint sensitivities. To facilitate a smooth shape update during



**Figure 5.** Sensitivities obtained at 19 positions from second-order finite-difference studies using three different step sizes  $\Delta n$  for the single-phase flow over a bump in a channel: (a) FD sensitivities of the drag force and (b) FD sensitivities of the lift force.



**Figure 6.** Comparison of FD-sensitivities and adjoint sensitivities obtained with (Adj. B) and without (Adj. A) the adjoint advection term  $ADV_{R_i}^w$  for the single-phase flow over a bump in a channel; (a) sensitivities of the drag force and (b) sensitivities of the lift force.

optimisation studies, it is usually advised to perform a regularisation step – often labeled Sobolev-filtering – for the adjoint sensitivities. This aims to transfer the computed (rough) sensitivities into the (inherently smooth) desired gradient of the objective function using the Laplace–Beltrami operator (Bletzinger 2014; Stück and Rung 2011). The applications discussed in Section 4 inherit the regularisation of the adjoint sensitivities by an efficient first-order accurate regularisation technique introduced by Kröger and Rung (2015) and Kröger (2016).

In preparation of the application cases presented in Section 4, the importance of the advective fluxes and the influence of the consistency of the adjoint convective flux approximation is investigated. Attention is restricted to the lift objective functional and primal flow simulations using a high-order upwind biased monotonicity-preserving QUICK scheme. Figure 7 indicates the predictive accuracy of the adjoint sensitivities for different numerical approaches. Adjoint results are displayed for one configuration, which uses a consistent monotonic QDICK scheme but does not consider the adjoint advection term  $ADV_{R_i}^w$  and five results obtained from simulations with the advection term utilising different flux blending approaches to the deferred correction terms of a QDICK scheme. A blending factor of  $\gamma = 0$  refers to a low-order adjoint downwind differencing scheme (DDS), whereas  $\gamma = 1$  refers to the consistent adjoint QDICK approach.

Neglecting the advection term while still employing a high-order convection scheme results in a maximum error of more than 60% (dashed line in Figure 7). On the contrary, a fair predictive accuracy is seen provided that the advection term is considered. The result is intriguing as some authors neglect the advection term (e.g. Soto and Löhner 2004). The maximum deviation between high- and low-order approximations of convective kinematics occurs in the region of the

maximum sensitivity but never exceeds 4%. The related Peclet-numbers are small but not negligible ( $O(1)$ ), particularly not in the tangential direction. Hence, the error caused by a slightly reduced order of the adjoint convection approximation is deemed small.

### 3.2. Two-phase simulations

The subsection is devoted to a comparison of sensitivities obtained from the adjoint VoF solver with results of second-order finite-difference studies for two-phase flows. All results refer to consistent high-order approximations for primal and adjoint momentum convection and a compressive HRIC scheme for the primal concentration, an implicit DDS approach

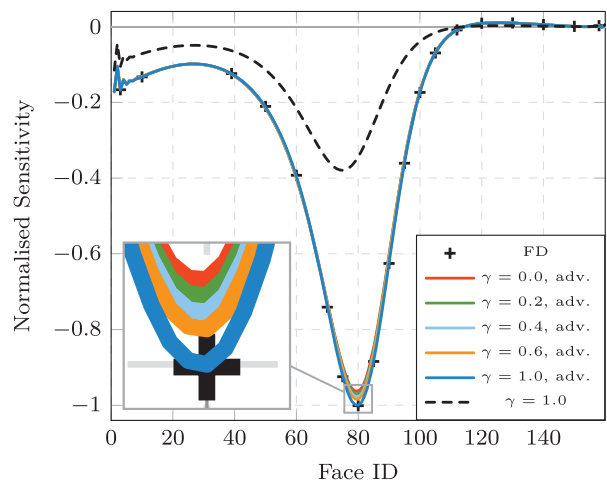


**Figure 7.** Normalised sensitivities returned by FD studies (FD) and different adjoint approximations. A value of  $\gamma = 0$  refers to implicit DDS approximation of the convection term,  $\gamma = 1$  denotes to a high-order QDICK scheme. The dashed black line denotes the sensitivities obtained with an adjoint high-order QDICK approximation while neglecting the advection term. The note *adv.* indicates that the advection term was considered.

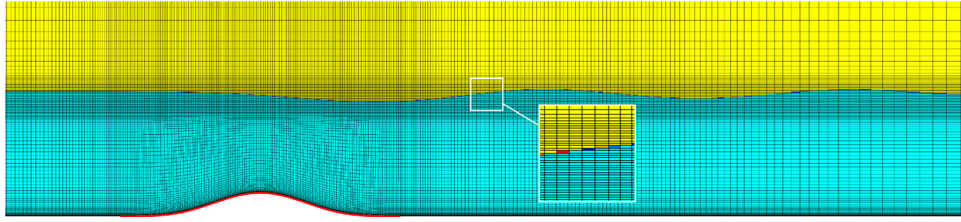


**Figure 8.** Concentration contours simulated for a two-phase flow over a bump in a channel at  $Fn = 0.555$ .

is utilised for the adjoint convective concentration transport. Emphasis is given to the impact of different adjoint coupling terms on the predictive accuracy. In addition, configurations with a deeply submerged design object and two-phase simulations with identical material properties are investigated to verify the correctness of the implementation.

The vertical position of the free surface at the inlet is set to 0.4 m above the bottom, relating to a depth-based Froude number of  $Fn = 0.555$ . The computational mesh is refined in the (anticipated) free surface region as illustrated in Figure 8. At this Froude number, the interaction between free-surface and design object produces a quasi-steady wave-field which is depicted in Figures 8 and 9, which also outline the fair performance of the compressive sharp-interface approach.

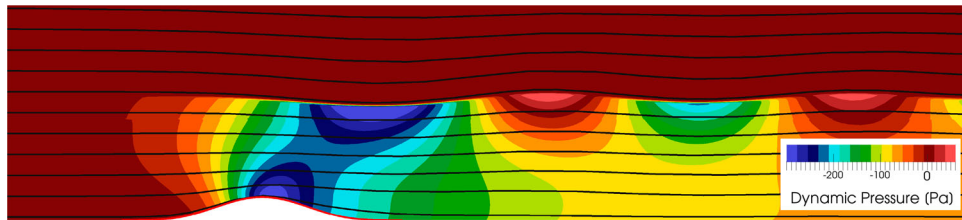
A systematic study on the influence of different step sizes on FD approaches is performed for the converged primal two-phase flow solution. Figure 10 displays the

sensitivities for four investigated step sizes, i.e.  $\Delta n$ ,  $\Delta n/2$ ,  $\Delta n/10$  and  $\Delta n/100$ . Apparently, the result of the smallest step size is inconsistent with results obtained for the three larger displacements.

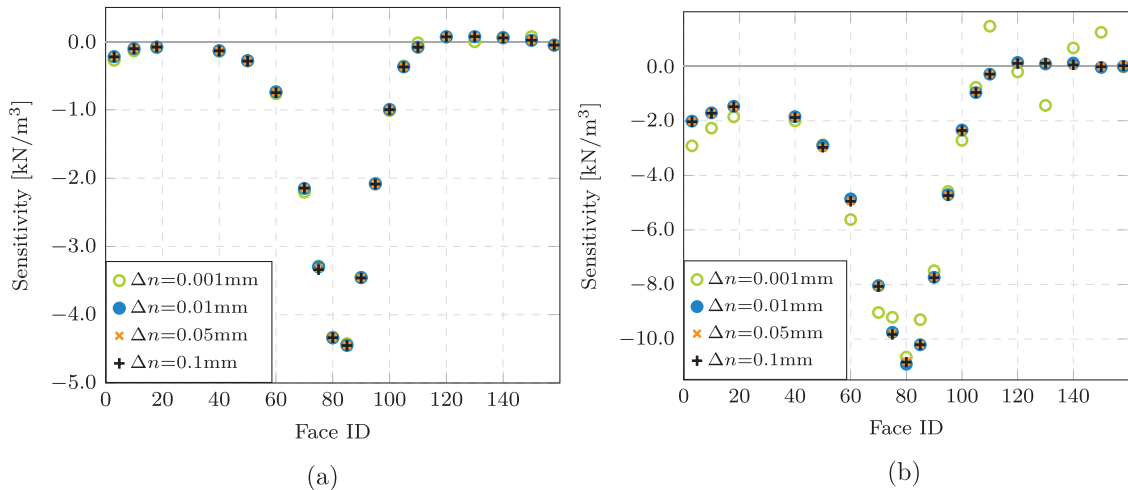
Following the finite-difference studies, the influence of the different coupling terms on the predictive accuracy of the adjoint two-phase solver is investigated.

Figure 11 compares the FD-sensitivities with the results from the following adjoint configurations (also summarised in Table 2):

- **A:** Adjoint solver without coupling the adjoint concentration into the adjoint momentum equation. Essentially, this is a frozen-concentration setup. Considers coupling terms between the adjoint momentum equations.
- **B:** Coupled adjoint two-phase flow solver, i.e. the adjoint concentration equation is coupled to the adjoint momentum equation and vice versa.



**Figure 9.** Streamlines and contours of the dynamic pressure simulated for a two-phase flow over a bump in a channel at  $Fn = 0.555$ .



**Figure 10.** Sensitivities obtained from second-order accurate FD-studies for four different step sizes  $\Delta n$  for the two-phase flow over a bump in a channel at  $Fn = 0.555$ : (a) sensitivities of the drag force and (b) sensitivities of the lift force.



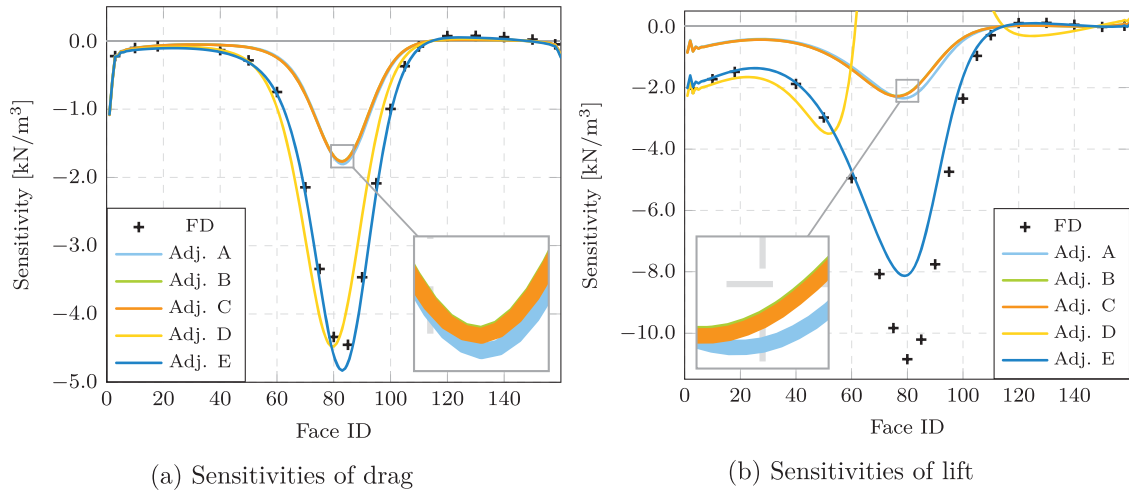


**Figure 11.** Comparison of sensitivities obtained from second-order FD-studies and from adjoint simulations (Adj. A–E) for the two-phase flow over bump in a channel at  $Fn = 0.555$ : (a) sensitivities of drag and (b) sensitivities of lift.

Considers coupling terms between the adjoint momentum equations. However, the adjoint concentration equation neglects the terms from the variation of the primal diffusion and the hydrostatic source term.

- **C:** Coupled adjoint two-phase solver, all coupling terms except the variation of the primal hydrostatic source are considered. An additional diffusion term is considered as part of the adjoint concentration equation.
- **D:** Coupled adjoint two-phase solver, all coupling terms except the cross-coupling of the adjoint momentum equations are considered. An additional diffusion term is considered as part of the adjoint concentration equation.
- **E:** Coupled adjoint two-phase solver with all coupling terms. An additional diffusion term is considered as part of the adjoint concentration equation.

All of the above configurations (Adj. A–E) consider the standard adjoint diffusion term as part of the adjoint momentum equations. The frozen-concentration approach (A) fails in predicting the FD-sensitivities as do the coupled configurations that neglect the advective term that originates from hydrostatics (B and C). Interestingly, these three configurations (A, B and C) lead to very similar results. Considering all advective terms except the cross-coupling term of the momentum equations (D) leads to reasonable

results for the resistance, although a phase shift can be observed. This configuration completely fails in predicting the sensitivities for the lift. The fully coupled configuration (E) shows an excellent agreement with the FD-sensitivities of the drag. For the objective lift, the sensitivities match the FD-sensitivities in the front and rear part of the design object while missing the magnitude of the sensitivities around the middle section of the design object. Still, the fully coupled adjoint solver returns significantly better sensitivity predictions than the frozen-concentration approach or strategies that neglect the term stemming from hydrostatics or the standard coupling term of the adjoint momentum equations. The sensitivities are correct in terms of their sign. In the context of gradient-based optimisation, the observed reduction in the magnitude translates into a reduced effective step size while still marching into the correct direction. The relevant advective terms for the adjoint two-phase flow solver are the hydrostatic term and the coupling between the momentum equations. The term originating from the primal momentum diffusion term that contributes to the adjoint concentration equation has no significant impact on the predicted sensitivities.

The adjoint configurations C–E include an additional diffusive transport term for the adjoint concentration balance. The heuristic term has been introduced to increase the robustness of the numerical method, which seems necessary for the complex applications presented in Section 4. As discussed above, the various coupling terms constitute a strong explicit coupling of the adjoint system. Robustness issues are in particular experienced in combination with the variation of the primal hydrostatic momentum source  $HYDR_{R_i}^{p'}$  in Equation (17). The term inheres the adjoint momentum and scales with the density difference. Configurations with a hydrodynamic force criterion and the associated adjoint boundary velocity being aligned with the gravity vector are particularly

**Table 2.** Adjoint two-phase flow configurations applied to the flow over a bump in a channel.

	Adj. A	Adj. B	Adj. C	Adj. D	Adj. E
$DIFF_{R_i}^{u'}$	×	×	×	×	×
$ADV_{R_i}^{u'}$	×	×	×	×	×
$ADV_{R_i}^{p'}$		×	×	×	×
$ADV_{R_i}^C$		×	×	×	×
$DIFF_{R_i}^{u'}$			×	×	×
$HYDR_{R_i}^{p'}$				×	×
$DIFF_{R_i}^C$			×	×	×

challenging. The coupling term leads to a strong adjoint concentration source directly above the design surface and inhibits convergence in the initial phase of the segregated iterative solution process.

To improve the resolution of strong gradients (discontinuities) with the available discretisation modules, the equation is manipulated by introducing an implicitly treated diffusive transport term  $\text{DIFF}^{\hat{c}}$  to the adjoint concentration equation, i.e.

$$\text{DIFF}^{\hat{c}} = \nu_{\hat{c}} \frac{\partial^2 \hat{c}}{\partial x_k^2} \quad (34)$$

The strategy essentially borrows an element from a diffusive interface model, e.g. the Cahn–Hilliard models described by Hinze and Kahle (2013), but deliberately violates the adjoint consistency for the diffusion transport of  $c$ . A comparison between configuration D and E indicates small differences from diffusion terms in the context of momentum transport. The revised non-dimensional adjoint concentration equation (cf. Section 2.3) reads

$$\begin{aligned} -\frac{L}{VT} \frac{\partial \hat{c}^*}{\partial t^*} - u_k^* \frac{\partial \hat{c}^*}{\partial x_k^*} &= \frac{\rho_{\Delta} V}{\hat{C}} \left[ -\hat{u}_i u_k^* \frac{\partial u_i^*}{\partial x_k^*} \right. \\ &\quad \left. - \left( \frac{\mu_{\Delta}}{\rho_{\Delta} V L} \right) 2S_{ik}^* \frac{\partial \hat{u}_i}{\partial x_k^*} + \left( \frac{Lg}{V^2} \right) \hat{u}_i g_i^* + \left( \frac{\nu_{\hat{c}} \hat{C}}{\rho_{\Delta} V^2 L} \right) \frac{\partial^2 \hat{c}^*}{\partial x_k^{*2}} \right] \end{aligned} \quad (35)$$

The implicitly treated diffusive transport term becomes insignificant for large velocities and mild curvature. For low-speed cases ( $V \rightarrow 0$ ), it balances the strong hydrostatic contribution, regularises the adjoint concentration equation and provides the necessary smoothness of the approximated solution.

Including an artificial term in the adjoint equation system obviously raises the question whether the sensitivities predicted by the adjoint solver are

significantly affected. A systematic parameter study is conducted for the coupled adjoint two-phase solver. To ensure convergence regardless of the diffusive term both the advective terms from primal diffusion and hydrostatic were neglected (configuration B). The impact of the additional diffusive term is studied for diffusion coefficients  $\nu_{\hat{c}}$  between zero and  $\nu_{\hat{c}} = 0.1 \text{ m}^2/\text{s}$ . The unit of the diffusion coefficient is determined from the Lagrangian; hence, it depends on the utilised objective functional. For the fully coupled adjoint configuration discussed above, a diffusion coefficient of  $\nu_{\hat{c}} = 1.0 \cdot 10^{-4} \text{ m}^2/\text{s}$  is sufficient to ensure convergence. Here, the maximum observed local deviation in the sensitivities lies well below 1% of the sensitivities of both the resistance and the lift (cf. Figure 12).

In addition to the previously presented results supplemental plausibility studies were performed. For deeply submerged configurations without interaction between the design object and the free water surface, the predicted sensitivities are expected to be identical to the results calculated for a single-phase setup. Another test case inheres a two-phase setup with interaction between the free surface and the design object. Here, both fluid phases are assigned identical material properties. The predicted sensitivities are expected to be identical to those obtained from a single-phase simulation. The evaluation of both studies agrees with the expected results.

#### 4. Hull optimisation for total resistance

This section reports on the application of the adjoint two-phase solver to a practically relevant case. The considered ship hull refers to the Kriso container ship (KCS). The test case was part of several international workshops that focused on the assessment of

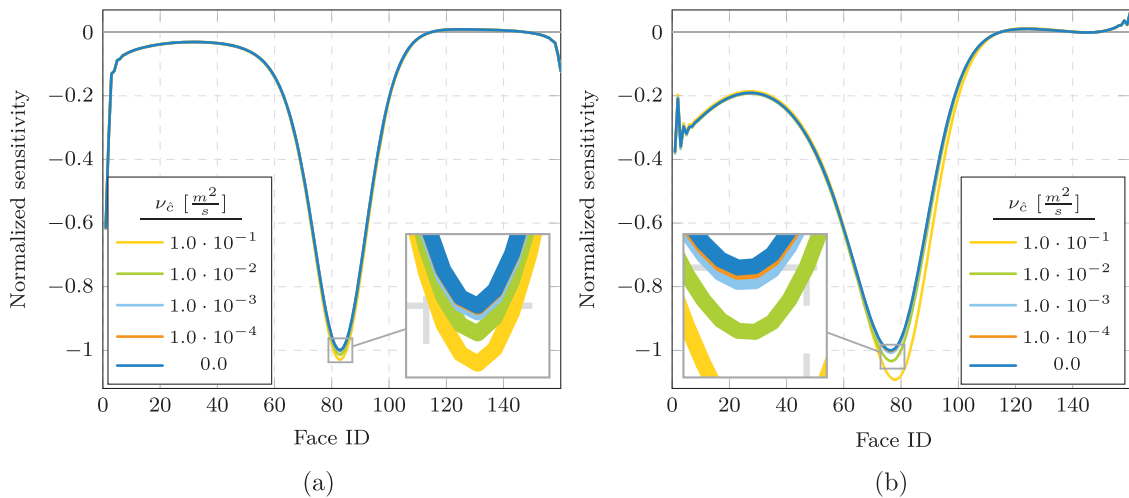


**Figure 12.** Influence of the intensity of an additional adjoint diffusive concentration transport on the predictive accuracy for the two-phase flow over a bump in a channel using different diffusion coefficients  $\nu_{\hat{c}}$ . Sensitivities are normalised with the maximum sensitivity (magnitude) for  $\nu_{\hat{c}} = 0 \text{ m}^2/\text{s}$ : (a) normalised sensitivities of drag and (b) normalised sensitivities of lift.



**Figure 13.** Buttock lines of the initial KCS hull.

hydrodynamic simulation procedures (e.g. Larsson et al. 2013) and offers a large body of numerical and experimental reference data. The investigated initial configuration refers to experimental calm-water studies conducted by Kim et al. (2001) and was previously computed under the aegis of case 2.1 during the Gothenburg 2010 workshop (Larsson et al. 2013). The buttock lines of the initial geometry are depicted in Figure 13.

The length of the investigated bare hull model is  $L_{pp} = 7.2786$  m. Present computations and experiments were carried out at a Froude number of  $Fn = 0.260$  and a Reynolds number of  $Re = 1.4 \cdot 10^7$  with a corresponding velocity of  $v_m = 2.196$  m/s. The model was trimmed to even keel and dynamic trim and sinkage were suppressed during the experiments and computations. The model was towed without propulsion, a dummy boss cap was placed in the stern tube.

The assessment of results refers to the following coordinate system: the origin is located in the aft perpendicular (AP) on baseline (BL) and centreline (CL). All coordinates are normalised with  $L_{pp}$ , i.e. the forward perpendicular FP is located at  $x/L_{pp} = 1.0$ .

#### 4.1. Computational model

The computational mesh comprises 5.7 million unstructured hexahedral cells. The extensions of the domain are  $5 \times L_{pp}$  in the longitudinal ( $x$ ),  $1.75 \times L_{pp}$  in the lateral ( $y$ ) and  $2.5 \times L_{pp}$  in the vertical ( $z$ ) direction. Due to symmetry, only half of the ship is modelled in the lateral direction. The inlet plane is located at  $x/L_{pp} = 3$  and the calm-water surface is

initialised at  $z = 0.3418$  m ( $1.75 \times L_{pp}$  above the lower boundary of the domain).

The hull is discretised with 140,000 surface elements. The surface-normal resolution of  $l_n = 4 \cdot 10^{-3}$  m ( $l_n/L_{pp} = 5 \cdot 10^{-4}$ ) yields  $y^+$ -values in the range of 30–150, which justifies the use of wall functions along the hull. A typical tangential cell spacing for the hull reads  $l_t = 8 \cdot 10^{-3}$  m ( $l_t/L_{pp} = 1 \cdot 10^{-3}$ ). The continuously fine surface discretisation is chosen to ensure an adequate resolution of unknown features of an optimised hull even in regions of initially low curvature. The vertical resolution of the free-surface region is identical throughout the domain and is related to the expected wave amplitudes of approximately 0.04 m ( $z/L_{pp} \approx 0.005$ ) close to the hull. Accordingly, the wave amplitude is resolved with 10 cells. The tangential resolution of the free-surface region is refined within a Kelvin-wedge to capture the wave field generated by the ship. The horizontal ( $x, y$ ) resolution within the Kelvin-wedge of  $l_x = l_y = 0.032$  m is adjusted to the ships characteristic wavelength  $\lambda_w = 2\pi/gv_m^2 = 3.09$  m that is resolved by approximately 100 cells. In the far field, the aspect ratio within the free-surface region is successively increased while maintaining the vertical resolution, cf. Figure 14. Since the adjoint convective transport is directed against the primal convective transport, the mesh is also refined upstream of the ship.

A uniform velocity profile is imposed at the inlet boundary. The pressure at the outlet is assigned to the hydrostatic pressure, all other quantities are extrapolated with zero gradient. Along the midships plane a symmetry condition is declared. Wall functions

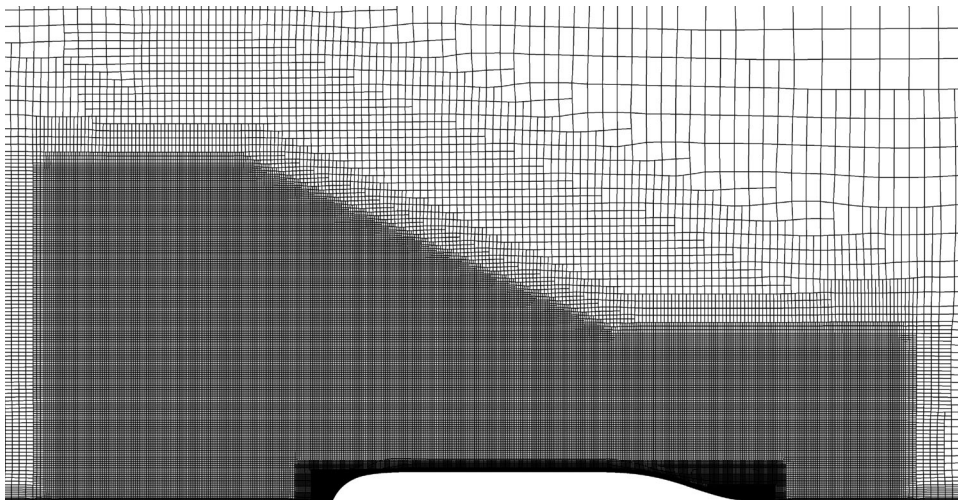


**Figure 14.** Optimisation of the KCS container ship ( $Fn = 0.260$ ,  $Re = 1.4 \cdot 10^7$ ); Computational mesh in the vicinity of the ship hull. Horizontal slice in the still water plane.



were used along the hull. The remaining boundaries are considered as slip-walls.

The time step for the implicit Euler scheme is 0.01 s which corresponds to a Courant number of 0.68 based upon the inflow velocity and a typical horizontal mesh spacing of 0.032 m. The momentum balance uses a monotonicity-preserving QUICK-scheme. The concentration transport employs the HRIC scheme in conjunction with a sub-cycling approach to ensure the Courant number requirements of the free-surface model while allowing for an efficient global time step (cf. Manzke et al. 2013). The SST  $k$ - $\omega$  model is used to model turbulence. The simulation was stopped after integral forces on the hull converged to constant mean values.

#### 4.2. Primal flow results

The converged solution reveals a quasi-steady wave field as depicted in Figure 15. Only directly behind the transom a confined region with unsteady behaviour is observed.

The wave elevation along the hull shows minor deviations from the experimental observation (cf. Figure 16 (a)). This discrepancy is in line with many other contributors to the Gothenburg 2010 workshop. The experiments did face difficulties to accurately read the wave elevation along the hull, in particular in the vicinity of the stern overhang (namely Kim et al. 2001). Figures 16(b) and 17(a,b) indicate an excellent agreement between the wave field prediction and the experimental data. Even at greater lateral distances from the ship, all relevant features indicated by the

experimental data are resolved by the simulation. No significant wave damping can be observed downstream of the transom and the computational model is deemed adequate for an optimisation of the configuration. A first analysis of the wave field suggests that the design would benefit from an increase of the water line length to approach a Hollow-Froude number. For the given design, the wave troughs of the forward and aft shoulders are in reinforcing interference with the bow and stern wave systems. A relocation of the shoulders is thus advised to attenuate the reinforcing interference of the wave systems.

#### 4.3. Optimisation setup

The computed adjoint sensitivities drive a CAD-free optimisation procedure, which was previously described by Kröger and Rung (2015) and Kröger (2016), to reduce the total resistance of the hull.

The design surface comprises all parts of the hull that are potentially wetted. Additional constraints were imposed during the optimisation to secure the practical applicability of the shape modification. The related constraint management strategy is discussed in Kröger (2016). The following constraints were imposed during the present optimisation:

- Maintenance of
  - the initial (wetted) displacement.
  - maximum draft and maximum beam.
  - the planar character of the transom.

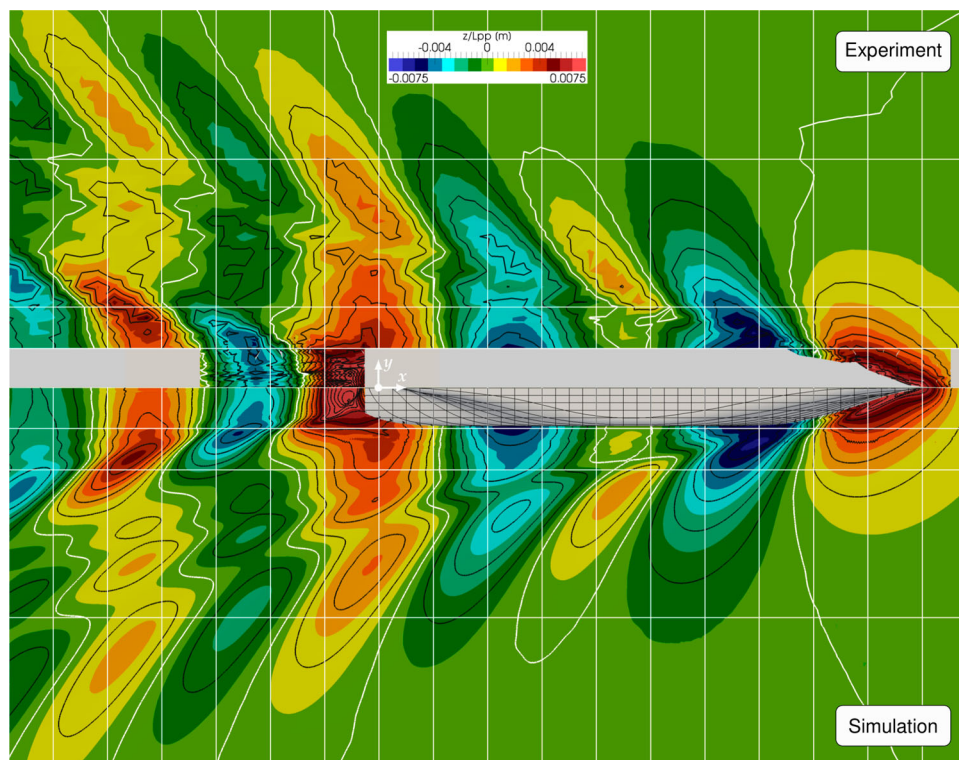


**Figure 15.** Optimisation of the KCS container ship ( $F_n = 0.260$ ,  $Re = 1.4 \cdot 10^7$ ); comparison of the measured (top, Kim et al. 2001) and computed (bottom) wave field in the vicinity of the hull.



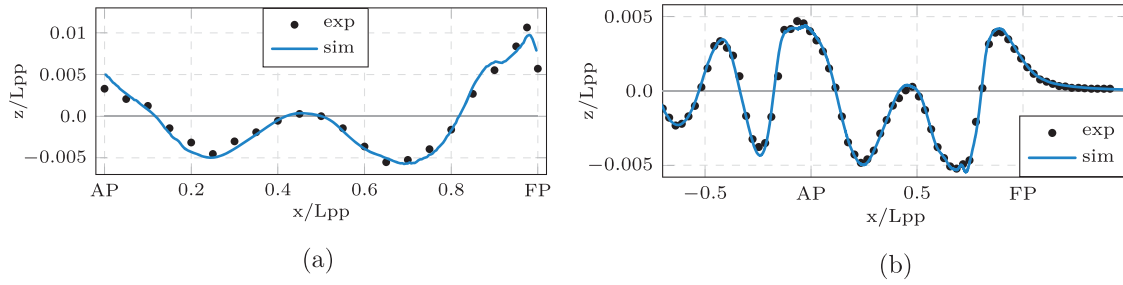


**Figure 16.** Optimisation of the KCS container ship ( $F_n = 0.260$ ,  $Re = 1.4 \cdot 10^7$ ); Wave elevation along hull and longitudinal wave profile at  $y/L_{pp} = 0.0741$  (experiments and simulation): (a) wave elevation along hull and (b) wave profile at  $y/L_{pp} = 0.0741$ .

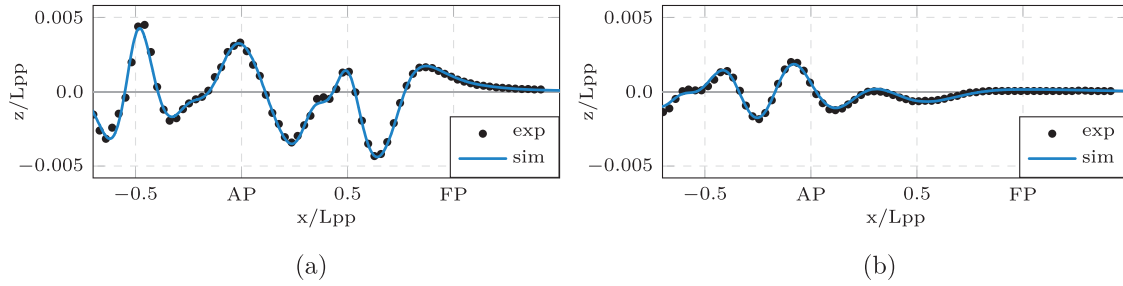


**Figure 17.** Optimisation of the KCS container ship ( $F_n = 0.260$ ,  $Re = 1.4 \cdot 10^7$ ); Longitudinal wave profiles at  $y/L_{pp} = 0.1509$  (a) and  $y/L_{pp} = 0.4224$  (b) (experiments and simulation).

- Preservation of domain boundaries that intersect with the design surface (symmetry at midship).
- Suppression of normal deformation in the vicinity of stern tube if directed towards the tube.

The computed shape sensitivities are transferred into the shape gradient during a post-processing step. The present study employs an explicit filtering procedure, which is a first-order approximation to the Laplace–Beltrami operator (Stück and Rung 2011). The approach requires the selection of a suitable *filter width*. The filter width controls the smoothness of the gradient and maps the sensitivities into shape modifications, which feature the desired level of curvature. A small filter width can resolve localised shape changes, whereas larger filters neglect small-scale modifications and maintain the character of the initial shape. This yields global shape modifications which can be attractive from a manufacturing point of view. Moreover, a smooth shape update supports the robustness of the optimisation and the conservation of the initial quality of the CFD-mesh during successive shape modifications. The present study considered three different filter widths, i.e.  $\sigma = 0.08$  m ( $\sigma/L_{pp} = 0.011$ ),  $\sigma = 0.10$  m ( $\sigma/L_{pp} = 0.014$ ) and  $\sigma = 0.12$  m ( $\sigma/L_{pp} = 0.017$ ). The smallest filter width refers to the width of the bulbous bow, the largest filter width reflects the vertical distance between the shaft and the base line. The spatial step size was chosen to lead to a maximum absolute normal deformation of  $\Delta n = 1.0 \cdot 10^{-3}$  m during the first optimisation steps which translates to 0.2% of the ships beam.

The optimisation procedure utilises restart capabilities. After obtaining the primal reference solution and performing the first adjoint simulation, all consecutive primal and adjoint simulations are restarted from the respective preceding simulation. The adjoint solver is run in pseudo-unsteady mode to facilitate the convergence of the densely coupled adjoint equation system. The simulated time-frame per optimisation step corresponds to roughly three flow-passages to meet the convergence criteria. The adjoint concentration field is supplemented by the additional diffusive transport as discussed in Section 3 and all adjoint coupling terms are included.

#### 4.4. Optimisation results

Figures 18 summarises the evolution of the total resistance and its pressure and friction components. The observed reduction of the total resistance corresponds to approximately 5% for the smallest filter width of  $\sigma = 0.08$  m and above 3% for the largest filter width of  $\sigma = 0.12$  m. The reduction in frictional resistance is between 0.5% and 2%. A significant reduction is observed for the pressure resistance. Here, the smallest filter width leads to a reduction of almost 20% while the largest filter width yields a decrease of 15%.

The wave field displayed in Figure 19 indicates an overall reduction of the wave elevation. The reinforcing interference of the bow wave trough with the wave trough of the forward shoulder is disturbed for the optimised shape. The pronounced, combined wave trough is now split into two dedicated troughs where

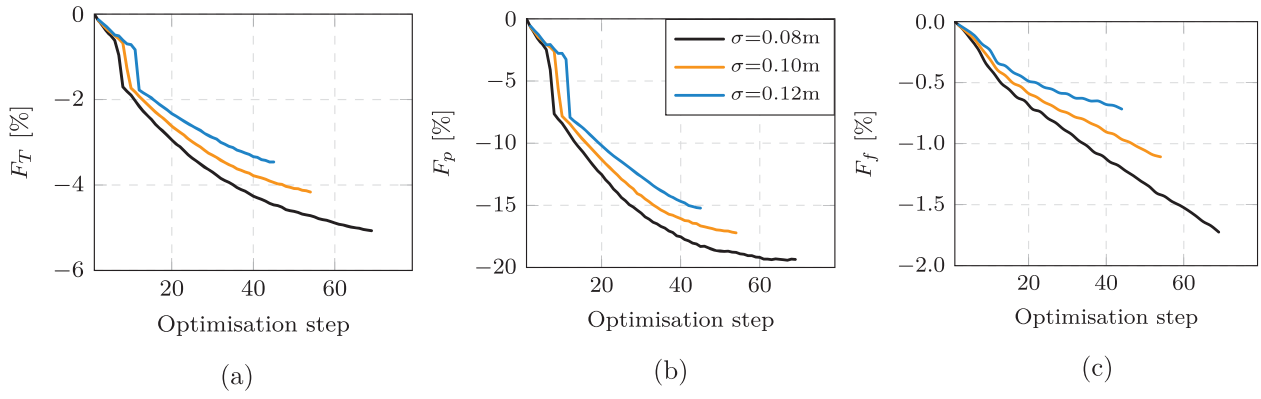


**Figure 18.** Evolution of the total resistance (a) and its pressure (b) and friction components (c) during the optimisation of the KCS hull using three different filter widths ( $F_n = 0.260$ ,  $Re = 1.4 \cdot 10^7$ ).

the shoulder trough tends aftwards and the bow wave trough is moderately shifted forward (at symbol ① in Figure 19). The wave trough at the aft shoulder is reduced, a shift towards the bow is observed (at symbol ② in Figure 19). The wave crest behind the transom is reduced, during the optimisation the wave reattaches to the transom. The amplitude of the wave system aft of the transom is significantly reduced.

Figures 20 and 21 compare the wave elevation for different longitudinal wave cuts with the respective initial wave field along the hull and in the wake. The evaluated wake positions are indicated by the white grid lines in Figure 19.

The longitudinal wave profiles for different transversal offsets, i.e.  $y/L_{pp} = 0.0741$ ,  $y/L_{pp} = 0.1$  and

$y/L_{pp} = 0.1509$ , shown in Figure 21 confirm the overall reduction in wave elevation. When focusing on the wave elevation along the ships hull (cf. Figure 20(a)), it appears that the height of the bow wave crest reveals a slight increase and extends further in the upstream direction. At  $x/L_{pp} = 0.85$  a clear reduction of the bow wave is observed. Besides, the depth of the wave trough at both the forward and the aft shoulder is significantly reduced.

Figure 22 depicts the contour plot of the dynamic static pressure coefficient  $c_p = (p - p_{ref} - \rho g z) / (\rho / 2 v_m^2)$ , where  $p_{ref}$  denotes the reference pressure at the position of the free surface and  $z$  indicates the distance from the free surface. The initial geometry shows a distinct low-pressure patch along the side of the bulbous bow. Both

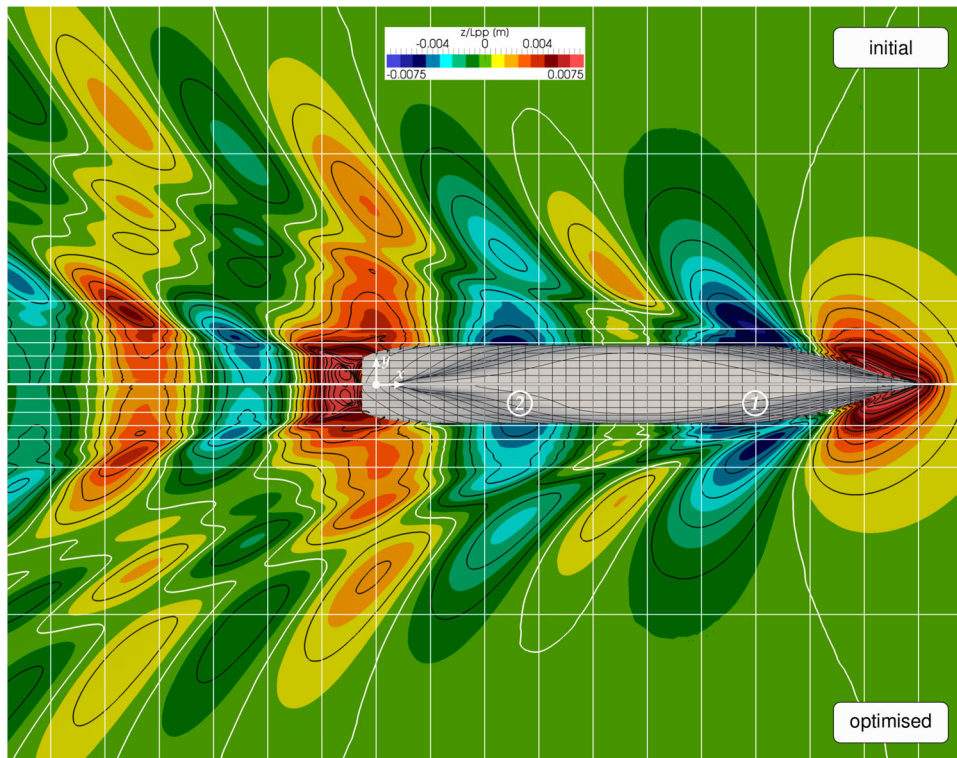


**Figure 19.** Comparison of initial (top) and optimised (bottom) wave fields in the vicinity of the hull for the KCS study ( $F_n = 0.260$ ,  $Re = 1.4 \cdot 10^7$  – optimisation refers to a filter width of  $\sigma = 0.08$  m).

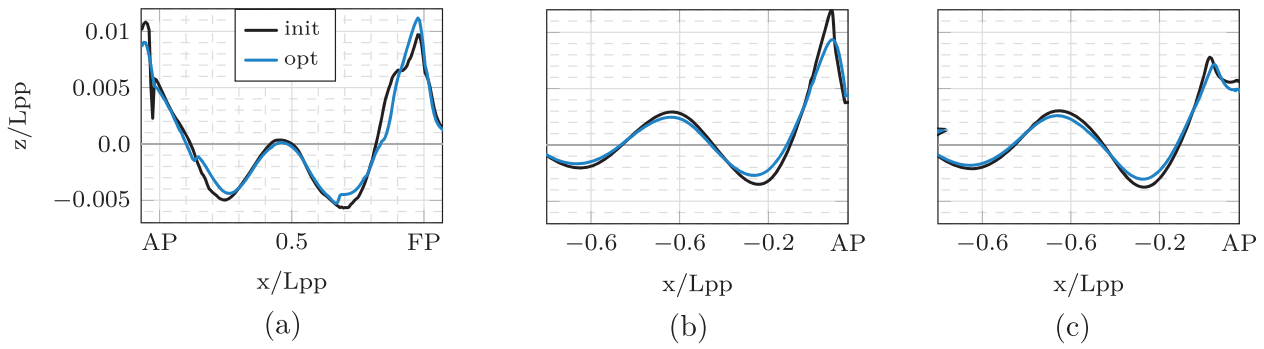


**Figure 20.** Comparison of predicted wave pattern for the initial and optimised hull of the KCS at  $F_n = 0.260$ ,  $Re = 1.4 \cdot 10^7$ , obtained with a filter width of  $\sigma = 0.08$  m. Wave elevation along hull (a) and longitudinal wave profiles behind the transom at two lateral positions, i.e. (b)  $y/L_{pp} = 0.025$ , (c)  $y/L_{pp} = 0.05$ . (a) Wave elevation along hull, (b) wave elevation in the wake at  $y/L_{pp} = 0.025$  and (c) wave elevation in the wake at  $y/L_{pp} = 0.05$ .

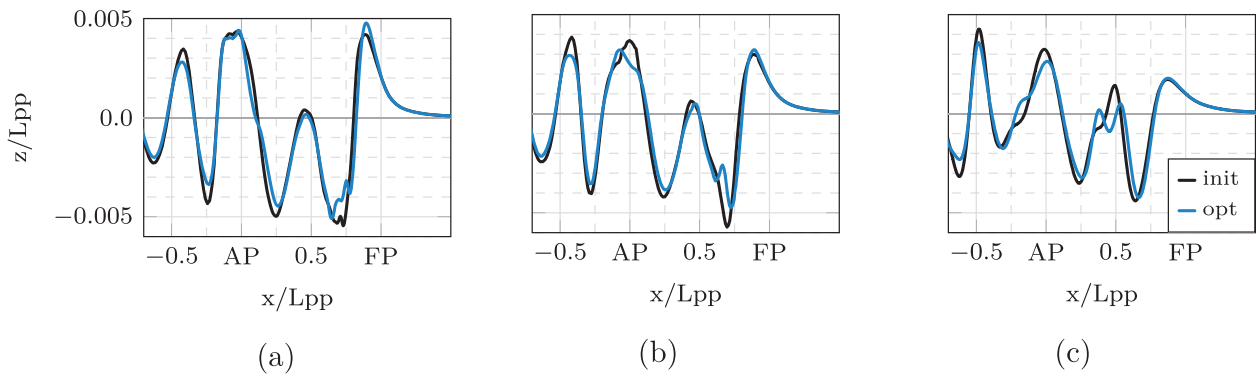


**Figure 21.** Comparison of predicted wave pattern for the initial and optimised hull of the KCS at  $F_n = 0.260$ ,  $Re = 1.4 \cdot 10^7$ , obtained with a filter width of  $\sigma = 0.08$  m. Longitudinal wave profiles at three lateral positions, i.e. (a)  $y/L_{pp} = 0.0741$ , (b)  $y/L_{pp} = 0.1$  and (c)  $y/L_{pp} = 0.1509$ .

the smallest and the largest filter widths reduce the fullness of the bulbous bow, in particular for its lower sections. Still, the upper side of the bulbous bow shows a confined patch of low pressure. Since the bulbous bow is moved upwards towards the waterline, this patch of low pressure successively approaches the free surface. The extent of the low-pressure regions initially observed at both the forward and aft shoulder is reduced. The low-pressure patch at the forward shoulder moderately

moves aftwards while the corresponding patch at the aft shoulder moves towards the bow.

For both the smallest and the largest filter width, the initial and the optimised geometries are compared in Figures 23 and 24. Besides, the figures contain the initial and the optimised wave elevation along the hull. The bulbous bow is more slender and shifted significantly towards the free surface. Directly aft of the bulbous bow the fore ship is fuller than the initial

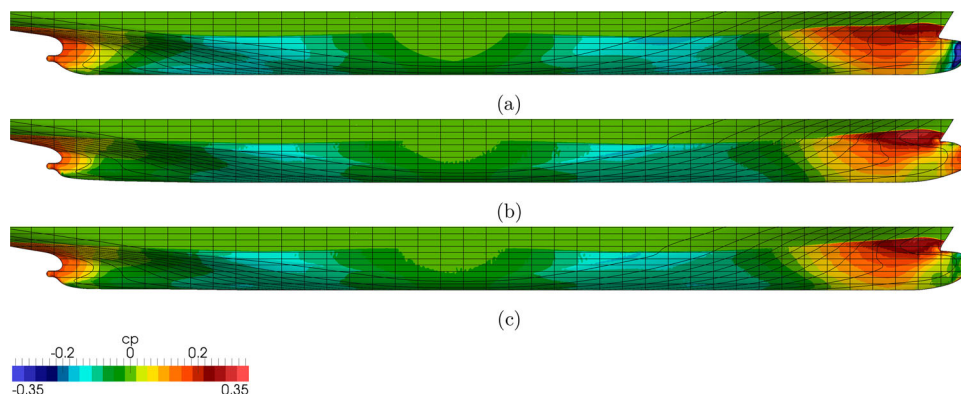


**Figure 22.** Optimisation of the KCS container ship hull at  $F_n = 0.260$ ,  $Re = 1.4 \cdot 10^7$ ; comparison of the initial geometry (a) with two optimal hulls (b,c) – obtained from different filter widths – the wetted part of the hull is coloured by contours of the dynamic static pressure coefficient.

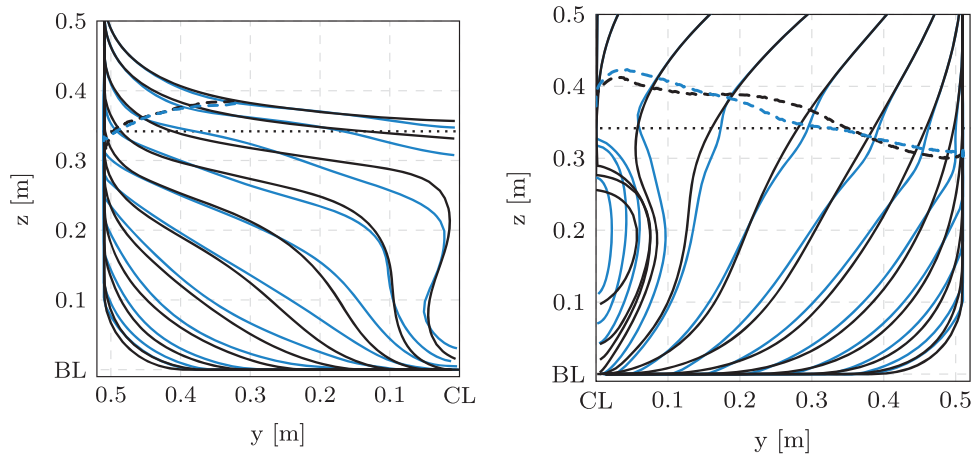


**Figure 23.** Optimisation of the KCS container ship hull at  $F_n = 0.260$ ,  $Re = 1.4 \cdot 10^7$ ; Frames plan for optimisation results obtained with a filter width of  $\sigma = 0.08$  m. Initial and optimised geometry indicated by continuous lines, initial and optimised wave elevation along the hull indicated by dashed lines (the color code follows figure 20). Still water line indicated as dotted line.

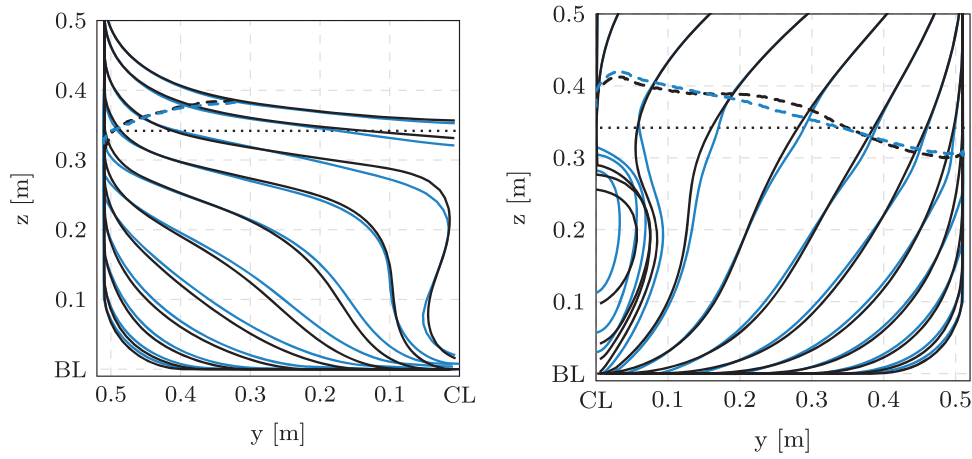


**Figure 24.** Optimisation of the KCS container ship hull at  $F_n = 0.260$ ,  $Re = 1.4 \cdot 10^7$ ; Frames plan for optimisation results obtained with a filter width of  $\sigma = 0.12$  m. Initial and optimised geometry indicated by continuous lines, initial and optimised wave elevation along the hull indicated by dashed lines (the color code follows figure 20). Still water line indicated as dotted line.

geometry, towards the forward shoulder the geometry is more slender than the initial configuration. The region around the aft shoulder is more slender, the same holds for the region below the shaft line. Above the shaft line, an increased fullness of the shape is observed. This is the result of the imposed displacement constraint. In this region, the sensitivity is small in comparison to the rest of the shape. Hence, the implemented displacement constraint utilises this region to balance the displacement. The relocation of displacement via the displacement constraint can have a significant impact on the longitudinal and vertical position of the centre of buoyancy. Future studies should thus also include the hydrostatic properties of the ship as constraints. For both the smallest and the largest filter width, the general characteristics of the observed shape modifications are comparable.

The optimisation leads to a significant reduction of the total resistance. Both the pressure and the frictional resistance are reduced while maintaining all declared constraints. The wave field shows a reduction of the

overall wave elevation. Interestingly, the shape modification inheres a reduction of the bulbous bow fullness, leading to a reduction of the low-pressure patch initially observed along the side of the bulbous bow. At the same time, the bulbous bow is re-positioned to reduce the distance between the low-pressure region on the upper side of the bulbous bow and the free surface. The shape manipulation successfully disturbs the reinforcing interference of the bow wave system and the wave system of the forward shoulder. Besides, a beneficial relocation of the wave systems created at the forward and aft shoulder is observed. The presented results address a specific operating point (single-point optimisation). To cover a wider range of operating conditions, the procedure can be embedded in a multi-point optimisation framework.

## 5. Conclusions

The paper reports on the development of an unstructured, segregated adjoint volume-of-fluid (VoF) solver,



which provides the sensitivities of an objective functional at the resolution of the discrete shape description. The procedure can be applied for industry-relevant shape optimisation problems.

The formulation of adjoint field equations and corresponding boundary conditions that constitute the adjoint two-phase problem follows the continuous adjoint approach. The discretisation of the adjoint PDE system was obtained from a hybrid continuous/discrete approach. Comparing to an adjoint single-phase flow problem, the adjoint two-phase flow PDE system inheres a number of additional terms that constitute a strong coupling. These terms can hinder the robustness of the segregated solver while having a significant impact on the predictive accuracy of the computed sensitivities. To facilitate the application in an industrial context, different stabilisation techniques were introduced. A diffusive concentration transport term was employed to attenuate local discontinuities in the adjoint concentration field and avoid singularities in hydrostatic conditions. A pseudo-unsteady mode was applied to provide an appreciated stabilisation of the adjoint solution process. Accordingly, all adjoint solutions were linearised around the same steady primal solution and converged to steady state. The adjoint convective transport is based on an implicit low-order downwind scheme supplemented by a high-order deferred-correction. A small damping of the related adjoint high-order convection terms was seen to stabilise the solution process at the cost of a minor reduction in the predictive accuracy of the adjoint solver.

A container ship hull was successfully optimised with regard to the total resistance. The relocation of the displacement lead to an overall reduction of the wave elevation. The observed resistance reduction involved the relocation of the bow wave system and the wave systems originating at the forward and aft shoulder and was achieved while maintaining the initial displacement and main dimensions.

## Disclosure statement

No potential conflict of interest was reported by the authors.

## Funding

The current work is a part of the research project *NoWelle* funded by the German Federal Ministry for Economic Affairs and Energy (BMWFi, grant no. 03FX362). Selected simulations were performed on the HLRN-III supercomputer system at the North German Cooperation for High-Performance computing (HLRN). All support is gratefully acknowledged by the authors.

## References

Armstrong CG, Robinson TT, Ou H, Othmer C. 2007. Linking adjoint sensitivity maps with CAD parameters.

- In: Neittaanmäki P, Périaux J, Tuovinen T, editors. *Evolutionary methods for design, optimization and control*. Barcelona, Spain: CIMNE.
- Bletzinger K-U. 2014. A consistent frame for sensitivity filtering and the vertex assigned morphing of optimal shape. *Struct Multidiscipl Optim*. 49(6):873–895.
- Ferziger JH, Perić M (2002). *Computational methods for fluid dynamics*. Berlin Heidelberg: Springer.
- Garcke H, Hinze M, Kahle C. 2016. A stable and linear time discretization for a thermodynamically consistent model for two-phase incompressible flow. *Appl Numer Math*. 99(C):151–171.
- Hinze M, Kahle C. 2013. A nonlinear model predictive concept for control of two-phase flows governed by the Cahn-Hilliard navier-stokes system. In Hömberg D, Tröltzsch F, editors. *25th System modeling and optimization (CSMO)*, Sep 2011, Berlin, Germany, IFIP advances in information and communication technology, AICT-391. System modeling and optimization. Springer; p. 348–357.
- Hirt CW, Nichols BD. 1981. Volume of Fluid (VOF) method for the dynamics of free boundaries. *J Comput Phys*. 39(1):201–225.
- Jameson A. 1988. Aerodynamic design via control theory. *J Sci Comput*. 3(3):233–260.
- Jameson A. 1995. Optimum aerodynamic design using CFD and control theory. AIAA-1995-1729-CP.
- Kim WJ, Van SH, Kim DH. 2001. Measurement of flows around modern commercial ship models. *Exp Fluids*. 31:567–578.
- Kröger J. 2016. A numerical process for the hydrodynamic optimisation of ships [PhD thesis]. Technische Universität Hamburg-Harburg.
- Kröger J, Rung T. 2015. CAD-free hydrodynamic optimisation using consistent kernel-based sensitivity filtering. *Ship Technol Res*. 62(3):111–130.
- Larsson L, Stern F, Visonneau M (2013). *Numerical ship hydrodynamics: an assessment of the Gothenburg 2010 workshop*. Dordrecht: Springer.
- Leonard BP. 1991. The ULTIMATE conservative difference scheme applied to unsteady one-dimensional advection. *Comput Methods Appl Mech Eng*. 88:17–74.
- Liu Z, Sandu A. 2005. Analysis of discrete adjoints for upwind numerical schemes. *Computational science – ICCS 2005: 5th international conference, Part II*; Atlanta, GA, USA. p. 829–836.
- Luo-Theilen X, Rung T. 2017. Computation of mechanically coupled bodies in a seaway. *Ship Technol Res*. accepted.
- Manzke M, Voss J-P, Rung T. 2013. Sub-cycling strategies for maritime two-phase flow simulations. *Notes Numer Fluid Mech Multidiscip Des*. 120:237–251.
- Martinelli L, Jameson A. 2007. An adjoint method for design optimization of ship hulls. 9th international conference on numerical ship hydrodynamics; Aug 5–8; Ann Arbor, MI.
- Martins JRR, Sturdza P, Alonso JJ. 2003. The complex-step derivative approximation. *ACM Trans Math Softw*. 29(3):245–262.
- Menter FR, Kuntz M, Langtry R. 2003. Ten years of industrial experience with the SST turbulence model. *Turbulence Heat Mass Transfer*. 4:625–632.
- Muzaferija S, Perić M. 1999. Computation of free-surface flows using interface-tracking and interface-capturing methods. In: Mahrenholtz O, Markiewicz M, editors. *Nonlinear water wave interaction, Chapter 2*. Southampton: WIT Press; p. 59–100.
- Nadarajah SK. 2003. The discrete adjoint approach to aerodynamic shape optimization [PhD thesis]. Stanford University.

- Newman III JC, Pankajakshan R, Whitfield DL, Taylor LK. 2002. Computational design optimization using RANS. 24th Symposium on naval hydrodynamics; Fukuoka, Japan.
- Othmer C. 2008. A continuous adjoint formulation for the computation of topological and surface sensitivities of ducted flows. *Int J Numer Meth Fluids*. 58(8):861–877.
- Othmer C. 2014. Adjoint methods for car aerodynamics. *Journal of Mathematics in Industry*. 4(6):1–23.
- Palacios F, Alonso JJ, Jameson A. 2012. Shape sensitivity of free-surface interfaces using a level set methodology. 42nd AIAA fluid dynamics conference and exhibit; Jun 25–28; New Orleans, LO.
- Palacios F, Alonso JJ, Jameson A. 2013. Design of free-surface interfaces using RANS equations. 43rd fluid dynamics conference – fluid dynamics and co-located conferences; Jun 24–27; San Diego, CA.
- Papoutsis-Kiachagias E, Zymaris A, Kavvadias I, Papadimitriou D, Giannakoglou K. 2015. The continuous adjoint approach to the  $k-\epsilon$  turbulence model for shape optimization and optimal active control of turbulent flows. *Eng Optim*. 47(3):370–389.
- Peter JE, Dwight RP. 2010. Numerical sensitivity analysis for aerodynamic optimization: a survey of approaches. *Comput Fluids*. 39(3):373–391.
- Pironneau O. 1974. On optimum design in fluid mechanics. *J Fluid Mech*. 64:97–110.
- Ragab SA. 2003 Aug. Shape optimization in free surface potential flow using an adjoint formulation. Naval Surface Warfare Center, Carderock Division, Hydrodynamics Directorate. Technical Report NSWCCD-50-TR-2003/33.
- Robinson T, Armstrong C, Chua H, Othmer C, Grahs T. 2012. Optimizing parameterized CAD geometries using sensitivities based on adjoint functions. *Comput Aided Des Appl*. 9(3):253–268.
- Rumsey C. 2014. NASA, Langley Research Center. Turbulence modeling resource: VERIF/2DB: 2D Bump-in-channel Verification Case. [accessed 2014 Nov 21]. <http://turbmodels.larc.nasa.gov/bump.html>.
- Rung T, Wöckner K, Manzke M, Brunswig J, Stück A, Ulrich C. 2009. Challenges and perspectives for maritime CFD applications. In: *Jahrbuch der Schiffbautechnischen Gesellschaft*. Vol. 103, Hamburg: Schiffahrts-Verlag “Hansa” GmbH & Co. KG; p. 127–139.
- Rusche H. 2002. Computational fluid dynamics of dispersed two-phase flows at high phase fractions [PhD thesis]. London: Imperial College of Science, Technology, and Medicine.
- So K, Hu X, Adams N. 2011. Anti-diffusion method for interface steepening in two-phase incompressible flow. *J Comput Phys*. 230(13):5155–5177.
- Söding H. 2001a. Practical hull shape design for reduced resistance. *Hydronav* 2001; Sep 27–29; Szczecin, Poland.
- Söding H. 2001b. Resistance decrease by computer-aided hull shape improvements. *HIPER* 2001; May 2–5; Hamburg.
- Söding H. 2001c. Hull shape design for reduced resistance. *Ship Technol Res*. 48(3):134–144.
- Soto O, Löhner R. 2004. On the computation of flow sensitivities from boundary integrals. 42nd AIAA aerospace sciences meeting and exhibit; Reno, NV. AIAA-04-0112.
- Soto O, Löhner R, Yang C. 2004. An adjoint-based design methodology for CFD problems. *Int J Numer Methods Heat Fluid Flow*. 14(6):734–759.
- Springer J. 2014. Multiphase adjoint optimization for efficient calculation of rigid body positions in Navier-Stokes flow [PhD thesis]. Universität Ulm.
- Stück A. 2012. Adjoint Navier-Stokes methods for hydrodynamic shape optimisation [PhD thesis]. Technische Universität Hamburg-Harburg.
- Stück A, Rung T. 2011. Adjoint rans with filtered shape derivatives for hydrodynamic optimisation. *Comput Fluids*. 47(1):22–32.
- Stück A, Rung T. 2013. Adjoint complement to viscous finite-volume pressure-correction methods. *J Comput Phys*. 248:402–419.
- Stück A, Camelli FF, Löhner R. 2010a. Adjoint-based design of shock mitigation devices. *Int J Numer Methods Fluids*. 64:443–472.
- Stück A, Kröger J, Rung T. 2010b. Adjoint RANS for Aftship design. V European conference on computational fluid dynamics ECCOMAS CFD; Jun 14–17; Lisbon, Portugal.
- Stück A, Kröger J, Rung T. 2011. Adjoint-based hull design for wake optimisation. *Ship Technol Res*. 58(1):34–44.
- Ubbink O. 1997. Numerical prediction of two fluid systems with sharp interfaces [PhD thesis]. University of London.
- van Leer B. 1979. Towards the ultimate conservative difference scheme. V. A second order sequel to Godunov's method. *J Comput Phys*. 32:101–136.
- Völkner S, Brunswig J, Rung T. 2017. Analysis of non-conservative interpolation techniques in overset grid finite volume methods. *Comput Fluids*. 148:39–55.
- Waclawczyk T, Koronowicz T. 2008. Comparison of CICSAM and HRIC high-resolution schemes for interface capturing. *J Theor Appl Mech*. 46(2):325–345.
- Yakubov S, Cankurt B, Abdel-Maksoud M, Rung T. 2013. Hybrid MPI/OpenMP parallelization of an Euler-Lagrange approach to cavitation modelling. *Comput Fluids*. 80:365–371.
- Yakubov S, Maquil T, Rung T. 2015. Experience using pressure-based CFD methods for Euler-Euler simulations of cavitating flows. *Comput Fluids*. 111:91–104.
- Zymaris A, Papadimitriou D, Giannakoglou K, Othmer C. 2009. Continuous adjoint approach to the Spalart-Allmaras turbulence model for incompressible flows. *Comput Fluids*. 38(8):1528–1538.